Online Supplement for
Sparse, Dense, and Compact Linearizations of the AC OPF*

Brent Eldridge[†1,2], Anya Castillo[‡3], Bernard Knueven[§4] and Manuel Garcia[¶3]

[1]Johns Hopkins University, Baltimore, MD 21218
[2]Federal Energy Regulatory Commission, Washington, DC 20426
[3]Sandia National Laboratories, Albuquerque, NM 87185
[4]National Renewable Eneregy Laboratory, Golden, CO 80401

December 1, 2020

Abstract

This document is an online supplement for [1]. Here we present complete derivations of the formulations examined, details of the lazy constraint algorithm, and full computational results supporting [1].

Nomenclature

Lowercase will denote decision variables, uppercase will denote parameters, bold will denote vectors and matrices, and plain typeface will denote scalar values.

*Funding provided by the U.S. Department of Energy's Office of Electricity Advanced Grid Modeling (AGM) program. The views presented are the personal views of the authors and not Federal Energy Regulatory Commission or any of its Commissioners. Sandia National Laboratories is a multimission laboratory managed and operated by National Technology and Engineering Solutions of Sandia, LLC, a wholly owned subsidiary of Honeywell International, Inc., for the U.S. Department of Energy's National Nuclear Security Administration under contract DENA0003525. This work was authored in part by the National Renewable Energy Laboratory, operated by Alliance for Sustainable Energy, LLC, for the U.S. Department of Energy (DOE) under Contract No. DE-AC36-08GO28308. The views expressed in the article do not necessarily represent the views of the DOE or the U.S. Government. The U.S. Government retains and the publisher, by accepting the article for publication, acknowledges that the U.S. Government retains a nonexclusive, paid-up, irrevocable, worldwide license to publish or reproduce the published form of this work, or allow others to do so, for U.S. Government purposes.

[†]brent.eldridge@ferc.gov
[‡]anya.castillo@gmail.com
[§]Bernard.Knueven@nrel.gov
[¶]mgarc19@sandia.gov

Sets

$\mathcal{K}$	Set of K transmission lines, $k \in \mathcal{K}$.
$\mathcal{K}_i$	Subset of $\mathcal{K}$ connected to bus i, $\mathcal{K}_i = \mathcal{K}_i^{fr} \cup \mathcal{K}_i^{to}$.
$\mathcal{K}_i^{fr}, \mathcal{K}_i^{to}$	Subset of $\mathcal{K}$ with "from" or "to" bus i.
$\mathcal{L}$	Set of L linearization sample points, $l \in \mathcal{L}$
$\mathcal{M}$	Set of M generators, $m \in \mathcal{M}$.
$\mathcal{M}_i$	Subset of $\mathcal{M}$ located at bus i.
$\mathcal{N}$	Set of N nodes or buses, $i, j, n \in \mathcal{N}$.
Ξ	Set of fixed solution variables $\xi \in \Xi$.

Parameters

τ_k	Transformer tap ratio on branch k.
ϕ_{ki}	Phase shifter from i-side of branch k.
$\mathbf{1}$	Appropriately sized vector of ones.
$\mathbf{A}$	Network incidence matrix, defined as $A_{ik} = 1$ and $A_{jk} = -1$ if $k \in \mathcal{K}_i^{fr} \cap \mathcal{K}_j^{to}$, and 0 otherwise.
B_{ik}^s	Shunt susceptance at i-side of branch k.
B_k	Susceptance of branch k.
C_m^y	Cost coefficients for generator m, $y \in \{0, 1, 2\}$.
$\mathbf{F}, \hat{\mathbf{F}}$	Real power flow sensitivities.
$\mathbf{F^0}, \hat{\mathbf{F}}^{\mathbf{0}}$	Real power flow offsets.
G_k	Conductance of branch k.
$\mathbf{H}, \hat{\mathbf{H}}$	Reactive power flow sensitivities.
$\mathbf{H^0}, \hat{\mathbf{H}}^{\mathbf{0}}$	Reactive power flow offsets.
$\mathbf{I}$	Identity matrix.
$\mathbf{K}, \hat{\mathbf{K}}$	Reactive power loss sensitivities.
$\mathbf{K^0}, \hat{\mathbf{K}}^{\mathbf{0}}$	Reactive power loss offsets.
$\check{\mathbf{K}}$	System-wide reactive power loss sensitivity.
$\check{K}^0$	System-wide reactive power loss offset.
$\mathbf{L}, \hat{\mathbf{L}}$	Real power loss sensitivities.
$\mathbf{L^0}, \hat{\mathbf{L}}^{\mathbf{0}}$	Real power loss offsets.
$\check{\mathbf{L}}$	System-wide real power loss sensitivity.
$\check{L}^0$	System-wide real power loss offset.
$\mathbf{P^d}, \mathbf{Q^d}$	Real and reactive power demand.
$\overline{\mathbf{P}}, \underline{\mathbf{P}}$	Max/min real power output.
$\overline{\mathbf{Q}}, \underline{\mathbf{Q}}$	Max/min reactive power output.
$\hat{\mathbf{S}}_\theta$	Voltage angle sensitivity to real power.
$\hat{\mathbf{S}}_\mathbf{v}$	Voltage magnitude sensitivity to reactive power.
$\hat{\mathbf{S}}_\theta^\mathbf{0}, \hat{\mathbf{S}}_\mathbf{v}^\mathbf{0}$	Voltage angle offsets.
$\overline{\mathbf{T}}$	Max power transfer limit.
$\overline{\mathbf{V}}, \underline{\mathbf{V}}$	Max/min voltage magnitude limit.

Variables

$\vec{\theta}$	Voltage phase angle.
$\mathbf{p^f}, \mathbf{p^t}$	Real power flow in the "from" and "to" directions.
$\mathbf{p^{f\alpha}}, \mathbf{p}^\ell$	Mid-line real power flow and branch line losses.
$\mathbf{p^g}, \mathbf{p^{nw}}$	Real power generation and net withdrawals.
p^ℓ	System-wide real power loss.
$\mathbf{q^f}, \mathbf{q^t}$	Reactive power flow in the "from" and "to" directions.
$\mathbf{q^{f\alpha}}, \mathbf{q}^\ell$	Mid-line reactive power flow and branch line losses.
$\mathbf{q^g}, \mathbf{q^{nw}}$	Reactive power generation and net withdrawals.
q^ℓ	System-wide reactive power loss.
$\mathbf{v}$	Voltage magnitude.
z	Primal objective function.

Additional Notation

$\top$	Matrix or vector transpose.
$\lvert \cdot \rvert$	Element-by-element absolute value.
$\lVert \cdot \rVert_2$	L-2 norm.
z^*	Optimal solution.

A Mid-Line Power Flow Formulations

Reference [2] derives the real power analogs to the mid-line reactive power flow (3) and losses (4), which can be extended to include linear reactive power approximations. The mid-line flows are derived by selecting $\alpha \in [0, 1]$, where $\alpha = 0$ corresponds to a measurement taken at node i and $\alpha = 1$ to node j, and then defining $p_k^f(\alpha) = (1-\alpha)p_k^f - \alpha p_k^t$ to be the real power flow measurement along branch k at a position α. Mid-line power flow and line loss equations for real and reactive power are as follows.

$$p_k^{f\alpha} = \frac{1}{2} G_k \left(\tau_k^2 v_i^2 - \tau_k^2 v_j^2\right) - B_k \tau_k v_i v_j \sin\left(\theta_{ij} - \phi_{ki}\right) \tag{33a}$$

$$q_k^{f\alpha} = \frac{-1}{2} \left((B_k + B_{ki}^s)\tau_k^2 v_i^2 - (B_k + B_{kj}^s)\tau_k^2 v_j^2\right) - G_k \tau_k v_i v_j \sin(\theta_{ij} - \phi_{ki}) \tag{33b}$$

$$p_k^\ell = G_k \left(\tau_k^2 v_i^2 + v_j^2\right) - 2G_k \tau_k v_i v_j \cos\left(\theta_{ij} - \phi_{ki}\right) \tag{33c}$$

$$q_k^\ell = -\left(B_k + B_{ki}^s\right)\tau_k^2 v_i^2 - \left(B_k + B_{kj}^s\right)\tau_k v_j^2 + 2B_k \tau_k v_i v_j \cos\left(\theta_{ij} - \phi_{ki}\right) \tag{33d}$$

Equations (33a) and (33b) illuminate the intuition behind tight coupling of real power with voltage angles and reactive power with voltage magnitude used in the fast-decoupled load flow [3] since the sine function is the dominant term in (33a) and the difference of squared voltages is the dominant term in (33b).

Power balance equations (6) and (7b) are repeated below, for convenience.

$$\mathbf{p^{nw}} + \mathbf{A}^\top \mathbf{p^{f\alpha}} + \tfrac{1}{2}|\mathbf{A}|^\top \mathbf{p}^\ell = 0 \tag{34a}$$

$$\mathbf{q^{nw}} + \mathbf{A}^\top \mathbf{q^{f\alpha}} + \tfrac{1}{2}|\mathbf{A}|^\top \mathbf{q}^\ell = 0 \tag{34b}$$

A.1 Taylor Series Expansion

The sparse sensitivity matrices $(\mathbf{F}, \mathbf{H}, \mathbf{L}, \mathbf{K})$ and their offsets $(\mathbf{F^0}, \mathbf{H^0}, \mathbf{L^0}, \mathbf{K^0})$ are given from the first order Taylor series expansions of real and reactive power flow and line losses $(\mathbf{p^{f\alpha}}, \mathbf{q^{f\alpha}}, \mathbf{p}^\ell, \mathbf{q}^\ell$, respectively). As explained in [1], the Taylor series expansion assumes a base-point solution $(\vec{\theta}_\xi, \mathbf{v}_\xi)$, where $\xi \in \Xi$ denotes the set of feasible AC power flow solutions.

From (33a), the first-order Taylor series for real power mid-line flow $p_k^{f\alpha}$, assuming $\frac{\partial p_k^{f\alpha}}{\partial \mathbf{v}} = 0$, is given below:

$$\begin{aligned} p_k^{f\alpha} \approx\ & G_k \tau_k^2 \left(v_{\xi_i}^2 - v_{\xi_j}^2 \right)/2 \\ & - B_k \tau_k v_{\xi_i} v_{\xi_j} \sin(\theta_{\xi_{ij}} - \phi_{ki}) \\ & - B_k \tau_k v_{\xi_i} v_{\xi_j} \cos(\theta_{\xi_{ij}} - \phi_{ki})(\theta_{ij} - \theta_{\xi_{ij}}) \end{aligned} \tag{35}$$

Summing together the linear terms defines the sensitivity matrix $\mathbf{F}$, and summing the constant terms defines the offset vector $\mathbf{F^0}$.

$$F_{ki} := -B_k \tau_k v_{\xi_i} v_{\xi_j} \cos(\theta_{\xi_{ij}} - \phi_{ki}) \tag{36a}$$

$$F_{kj} := B_k \tau_k v_{\xi_i} v_{\xi_j} \cos(\theta_{\xi_{ij}} - \phi_{ki}) \tag{36b}$$

$$\begin{aligned} F_k^0 :=\ & G_k \tau_k^2 \left(v_{\xi_i}^2 - v_{\xi_j}^2 \right)/2 \\ & - B_k \tau_k v_{\xi_i} v_{\xi_j} \sin(\theta_{\xi_{ij}} - \phi_{ki}) \\ & + B_k \tau_k v_{\xi_i} v_{\xi_j} \cos(\theta_{\xi_{ij}} - \phi_{ki})(\theta_{\xi_{ij}}) \end{aligned} \tag{36c}$$

From (33b), the first-order Taylor series for reactive power mid-line flow $q_k^{f\alpha}$, assuming $\frac{\partial q_k^{f\alpha}}{\partial \vec{\theta}} = 0$, is given below:

$$\begin{aligned} q_k^{f\alpha} \approx\ & -\tau_k^2 \left((B_k + B_{ki}^s) v_{\xi_i}^2 - (B_k + B_{kj}^s) v_{\xi_j}^2 \right)/2 \\ & - G_k \tau_k v_{\xi_i} v_{\xi_j} \sin(\theta_{\xi_{ij}} - \phi_{ki}) \\ & - (B_k + B_{ki}^s) \tau_k^2 v_{\xi_i} (v_i - v_{\xi_i}) \\ & - G_k \tau_k v_{\xi_j} \sin(\theta_{\xi_{ij}} - \phi_{ki})(v_i - v_{\xi_i}) \\ & + (B_k + B_{kj}^s) \tau_k^2 v_{\xi_j} (v_j - v_{\xi_j}) \\ & - G_k \tau_k v_{\xi_i} \sin(\theta_{\xi_{ij}} - \phi_{ki})(v_j - v_{\xi_j}) \end{aligned} \tag{37}$$

Summing together the linear terms defines the sensitivity matrix $\mathbf{H}$, and summing the constant terms defines the offset vector $\mathbf{H^0}$.

$$\begin{aligned} H_{ki} := &- (B_k + B^s_{ki})\, \tau_k^2 v_{\xi_i} \\ &- G_k \tau_k v_{\xi_j} \sin(\theta_{\xi_{ij}} - \phi_{ki}) \end{aligned} \tag{38a}$$

$$H_{kj} := (B_k + B^s_{kj}) \tau_k^2 v_{\xi_j} - G_k \tau_k v_{\xi_i} \sin(\theta_{ij} - \phi_{ki}) \tag{38b}$$

$$\begin{aligned} H^0_k := &\ \tau_k^2 \left((B_k + B^s_{ki}) v_{\xi_i}^2 - (B_k + B^s_{kj}) v_{\xi_j}^2 \right) /2 \\ &+ G_k \tau_k v_{\xi_i} v_{\xi_j} \sin(\theta_{\xi_{ij}} - \phi_{ki}) \end{aligned} \tag{38c}$$

From (33c), the first-order Taylor series for real power losses p_k^ℓ, assuming $\frac{\partial p_k^\ell}{\partial \mathbf{v}} = 0$, is given below:

$$\begin{aligned} p_k^\ell \approx &\ G_k \tau_k^2 \left(v_{\xi_i}^2 + v_{\xi_j}^2 \right) - 2 G_k \tau_k v_{\xi_i} v_{\xi_j} \cos(\theta_{\xi_{ij}} - \phi_{ki}) \\ &+ 2 G_k \tau_k v_{\xi_i} v_{\xi_j} \sin(\theta_{\xi_{ij}} - \phi_{ki})(\theta_{ij} - \theta_{\xi_{ij}}) \end{aligned} \tag{39}$$

Summing together the linear terms defines the sensitivity matrix $\mathbf{L}$, and summing the constant terms defines the offset vector $\mathbf{L^0}$.

$$L_{ki} := 2 G_k \tau_k v_{\xi_i} v_{\xi_j} \sin(\theta_{\xi_{ij}} - \phi_{ki}) \tag{40a}$$

$$L_{kj} := -2 G_k \tau_k v_{\xi_i} v_{\xi_j} \sin(\theta_{\xi_{ij}} - \phi_{ki}) \tag{40b}$$

$$\begin{aligned} L^0_k := &\ G_k \tau_k^2 \left(v_{\xi_i}^2 + v_{\xi_j}^2 \right) \\ &- 2 G_k \tau_k v_{\xi_i} v_{\xi_j} \cos(\theta_{\xi_{ij}} - \phi_{ki}) \\ &- 2 G_k \tau_k v_{\xi_i} v_{\xi_j} \sin(\theta_{\xi_{ij}} - \phi_{ki})(\theta_{\xi_{ij}}) \end{aligned} \tag{40c}$$

From (33d), the first-order Taylor series for reactive power losses q_k^ℓ, assuming $\frac{\partial q_k^\ell}{\partial \vec{\theta}} = 0$, is given below:

$$\begin{aligned} q_k^\ell \approx &- (B_k + B^s_{ki})\, \tau_k^2 v_{\xi_i}^2 - \left(B_k + B^s_{kj}\right) \tau_k^2 v_{\xi_j}^2 \\ &+ 2 B_k \tau_k v_{\xi_i} v_{\xi_j} \cos(\theta_{\xi_{ij}} - \phi_{ki}) \\ &- 2\, (B_k + B^s_{ki})\, \tau_k^2 v_{\xi_i} (v_i - v_{\xi_i}) \\ &+ 2 B_k \tau_k v_{\xi_j} \cos(\theta_{\xi_{ij}} - \phi_{ki})(v_i - v_{\xi_i}) \\ &- 2 \left(B_k + B^s_{kj}\right) \tau_k^2 v_{\xi_j} (v_j - v_{\xi_j}) \\ &+ 2 B_k \tau_k v_{\xi_i} \cos(\theta_{\xi_{ij}} - \phi_{ki})(v_j - v_{\xi_j}) \end{aligned} \tag{41}$$

Summing together the linear terms defines the sensitivity matrix $\mathbf{K}$, and summing the constant terms defines the offset vector $\mathbf{K^0}$.

$$K_{ki} := -2\, (B_k + B^s_{ki})\, \tau_k^2 v_{\xi_i} + 2 B_k \tau_k v_{\xi_j} \cos(\theta_{\xi_{ij}} - \phi_{ki}) \tag{42a}$$

$$K_{kj} := -2 \left(B_k + B^s_{kj}\right) \tau_k^2 v_{\xi_j} + 2 B_k \tau_k v_{\xi_i} \cos(\theta_{\xi_{ij}} - \phi_{ki}) \tag{42b}$$

$$\begin{aligned} K^0_k := &\ (B_k + B^s_{ki})\, \tau_k^2 v_{\xi_i}^2 + \left(B_k + B^s_{kj}\right) \tau_k^2 v_{\xi_j}^2 \\ &- 2 B_k \tau_k v_{\xi_i} v_{\xi_j} \cos(\theta_{\xi_{ij}} - \phi_{ki}) \end{aligned} \tag{42c}$$

The above definitions can then be used to calculate the other power flow coefficients described in Section A.2.

A.2 Implicit Sensitivity Solutions

The D-LOPF and C-LOPF formulations are derived by substituting the linearized power flow constraints (33) into the power balance constraints (34), as shown below.

$$\mathbf{p^{nw}} + \mathbf{A}^\top \left(\mathbf{F}\vec{\theta} + \mathbf{F}^0\right) + \frac{1}{2}|\mathbf{A}|^\top \left(\mathbf{L}\vec{\theta} + \mathbf{L}^0\right) = 0 \tag{43a}$$

$$\mathbf{q^{nw}} + \mathbf{A}^\top \left(\mathbf{H}\mathbf{v} + \mathbf{H}^0\right) + \frac{1}{2}|\mathbf{A}|^\top \left(\mathbf{K}\mathbf{v} + \mathbf{K}^0\right) = 0 \tag{43b}$$

Solving (43a) and (43b) for $\vec{\theta}$ and $\mathbf{v}$, respectively, derives the following sensitivity matrices and offset vectors.

$$\hat{\mathbf{S}}_\theta := -\left(\mathbf{A}^\top\mathbf{F} + \frac{1}{2}|\mathbf{A}|^\top\mathbf{L}\right)^{-1} \tag{44a}$$

$$\hat{\mathbf{S}}_\mathbf{v} := -\left(\mathbf{A}^\top\mathbf{H} + \frac{1}{2}|\mathbf{A}|^\top\mathbf{K}\right)^{-1} \tag{44b}$$

$$\hat{\mathbf{S}}^\mathbf{0}_\theta := \hat{\mathbf{S}}_\theta\left(\mathbf{A}^\top\mathbf{F^0} + \frac{1}{2}|\mathbf{A}|^\top\mathbf{L^0}\right) \tag{44c}$$

$$\hat{\mathbf{S}}^\mathbf{0}_\mathbf{v} := \hat{\mathbf{S}}_\mathbf{v}\left(\mathbf{A}^\top\mathbf{H^0} + \frac{1}{2}|\mathbf{A}|^\top\mathbf{K^0}\right) \tag{44d}$$

The linear system in (43a) is singular, so solving (44a) is performed in the standard way by removing the reference bus column. The above definitions allow $\vec{\theta}$ and $\mathbf{v}$ to be expressed by linear expressions $\vec{\theta} = \hat{\mathbf{S}}_\theta\mathbf{p^{nw}} + \hat{\mathbf{S}}^\mathbf{0}_\theta$ and $\mathbf{v} = \hat{\mathbf{S}}^\theta_\mathbf{v}\mathbf{q^{nw}} + \hat{\mathbf{S}}^\mathbf{0}_\mathbf{v}$, which will be substituted into (33) to create analogous constraints for $\mathbf{p}^{\mathbf{f}\alpha}, \mathbf{q}^{\mathbf{f}\alpha}, \mathbf{p}^\ell$, and $\mathbf{q}^\ell$. Numerically dense reactive power sensitivity matrices were previously defined in (14) and are defined below along with the analogous real power sensitivities.

$$\hat{\mathbf{F}} := \mathbf{F}\hat{\mathbf{S}}_\theta, \quad \hat{\mathbf{H}} := \mathbf{H}\hat{\mathbf{S}}_\mathbf{v}, \quad \hat{\mathbf{L}} := \mathbf{L}\hat{\mathbf{S}}_\theta, \quad \hat{\mathbf{K}} := \mathbf{K}\hat{\mathbf{S}}_\mathbf{v} \tag{45}$$

As before, linearization offset constants are also defined.

$$\begin{aligned} \hat{\mathbf{F}}^\mathbf{0} &:= \mathbf{F}\hat{\mathbf{S}}^\mathbf{0}_\theta + \mathbf{F^0}, \quad \hat{\mathbf{H}}^\mathbf{0} := \mathbf{H}\hat{\mathbf{S}}^\mathbf{0}_\mathbf{v} + \mathbf{H^0}, \\ \hat{\mathbf{L}}^\mathbf{0} &:= \mathbf{L}\hat{\mathbf{S}}^\mathbf{0}_\theta + \mathbf{L^0}, \quad \hat{\mathbf{K}}^\mathbf{0} := \mathbf{K}\hat{\mathbf{S}}^\mathbf{0}_\mathbf{v} + \mathbf{K^0} \end{aligned} \tag{46}$$

The definitions in (45) rely on first solving the inverted matrices $\hat{\mathbf{S}}_\theta$ and $\hat{\mathbf{S}}_\mathbf{v}$. This can be a computationally time-consuming process, so an alternative is to calculate the sensitivity matrices implicitly by solving the following linear

systems.[1]

$$-\left(\mathbf{A}^\top\mathbf{F}+\frac{1}{2}|\mathbf{A}|^\top\mathbf{L}\right)^\top\hat{\mathbf{F}}^\top=\mathbf{F}^\top \tag{47a}$$

$$-\left(\mathbf{A}^\top\mathbf{H}+\frac{1}{2}|\mathbf{A}|^\top\mathbf{K}\right)^\top\hat{\mathbf{H}}^\top=\mathbf{H}^\top \tag{47b}$$

$$-\left(\mathbf{A}^\top\mathbf{F}+\frac{1}{2}|\mathbf{A}|^\top\mathbf{L}\right)^\top\hat{\mathbf{L}}^\top=\mathbf{L}^\top \tag{47c}$$

$$-\left(\mathbf{A}^\top\mathbf{H}+\frac{1}{2}|\mathbf{A}|^\top\mathbf{K}\right)^\top\hat{\mathbf{K}}^\top=\mathbf{K}^\top \tag{47d}$$

The voltage magnitude sensitivity can also be computed this way.

$$-\left(\mathbf{A}^\top\mathbf{H}+\frac{1}{2}|\mathbf{A}|^\top\mathbf{K}\right)^\top\hat{\mathbf{S}}_{\mathbf{v}}^\top=\mathbf{I}^\top \tag{47e}$$

Definitions for the offset coefficients $\hat{\mathbf{F}},\hat{\mathbf{H}},\hat{\mathbf{L}}$, and $\hat{\mathbf{K}}$ that do not depend on $\hat{\mathbf{S}}_\theta$ or $\hat{\mathbf{S}}_{\mathbf{v}}$ can then be obtained from equations (44), (45), and (46).

$$\hat{\mathbf{F}}^{\mathbf{0}}=\hat{\mathbf{F}}\left(\mathbf{A}^\top\mathbf{F}+\frac{1}{2}|\mathbf{A}|^\top\mathbf{L}\right)+\mathbf{F}^{\mathbf{0}} \tag{48a}$$

$$\hat{\mathbf{H}}^{\mathbf{0}}=\hat{\mathbf{H}}\left(\mathbf{A}^\top\mathbf{H}+\frac{1}{2}|\mathbf{A}|^\top\mathbf{K}\right)+\mathbf{H}^{\mathbf{0}} \tag{48b}$$

$$\hat{\mathbf{L}}^{\mathbf{0}}=\hat{\mathbf{L}}\left(\mathbf{A}^\top\mathbf{F}+\frac{1}{2}|\mathbf{A}|^\top\mathbf{L}\right)+\mathbf{L}^{\mathbf{0}} \tag{48c}$$

$$\hat{\mathbf{K}}^{\mathbf{0}}=\hat{\mathbf{K}}\left(\mathbf{A}^\top\mathbf{H}+\frac{1}{2}|\mathbf{A}|^\top\mathbf{K}\right)+\mathbf{K}^{\mathbf{0}} \tag{48d}$$

The dense real power flow definition can be proven to be isomorphically equivalent to the sparse definition, as shown below.

$$\mathbf{p}^{\mathbf{f}\alpha}=\hat{\mathbf{F}}\mathbf{p}^{\mathbf{nw}}+\hat{\mathbf{F}}^{\mathbf{0}} \tag{49a}$$

$$=\mathbf{F}\left(\hat{\mathbf{S}}_\theta\mathbf{p}^{\mathbf{nw}}+\hat{\mathbf{S}}_\theta^{\mathbf{0}}\right)+\mathbf{F}^{\mathbf{0}} \tag{49b}$$

$$\begin{aligned}=-\mathbf{F}&\left(\mathbf{A}^\top\mathbf{F}+\frac{1}{2}|\mathbf{A}|^\top\mathbf{L}\right)^{-1}\\&\left(\mathbf{p}^{\mathbf{nw}}+\mathbf{A}^\top\mathbf{F}^{\mathbf{0}}+\frac{1}{2}|\mathbf{A}|^\top\mathbf{L}^{\mathbf{0}}\right)+\mathbf{F}^{\mathbf{0}}\end{aligned} \tag{49c}$$

Note that equation (43a) can be rearranged:

$$\left(\mathbf{A}^\top\mathbf{F}+\frac{1}{2}|\mathbf{A}|^\top\mathbf{L}\right)\vec{\theta}=-\mathbf{p}^{\mathbf{nw}}-\mathbf{A}^\top\mathbf{F}^0-\frac{1}{2}|\mathbf{A}|^\top\mathbf{L}^0$$

[1] Since the systems for $\hat{\mathbf{F}}$ and $\hat{\mathbf{L}}$ are singular, they are solved by designating a reference bus and removing the column associated with that bus from the linear equations.

which simplifies (49c):

$$\mathbf{p}^{\mathbf{f}\alpha} = \mathbf{F}\vec{\theta} + \mathbf{F}^{\mathbf{0}} \tag{49d}$$

Similar equivalence can be drawn from the other power flow and loss definitions, but are omitted for brevity. The dense power flow constraints (16) and (17) are therefore equivalent to the sparse constraints (10) and (11).

The calculation of system loss sensitivity factors $\check{\mathbf{L}}$ and $\check{\mathbf{K}}$ in equation (19) depends on first computing explicit branch loss sensitivities $\hat{\mathbf{L}}$ and $\hat{\mathbf{K}}$. Instead, $\check{\mathbf{L}}$ and $\check{\mathbf{K}}$ can be also defined implicitly. These factors are equal to one minus the power supplied to the reference bus per unit injected at bus i, as shown below:

$$\check{\mathbf{L}} := \mathbf{1} - \frac{\partial p_R^{nw}}{\partial p_i^{nw}}, \quad \check{L}^0 := p_\xi^\ell - \check{\mathbf{L}}\check{\mathbf{p}}_\xi^{\mathbf{nw}}, \quad \check{\mathbf{K}} := \mathbf{1} - \frac{\partial q_R^{nw}}{\partial q_i^{nw}}, \quad \check{K}^0 := q_\xi^\ell - \check{\mathbf{K}}\check{\mathbf{q}}_\xi^{\mathbf{nw}} \tag{50}$$

The following linear systems define the marginal system line loss sensitivities and can be solved for $\check{\mathbf{L}}$ and $\check{\mathbf{K}}$.[2]

$$\left(\mathbf{A}^\top\mathbf{F} + \frac{1}{2}|\mathbf{A}|^\top\mathbf{L}\right)^\top \check{\mathbf{L}}^\top = \left(\mathbf{A}^\top\mathbf{F} + \frac{1}{2}|\mathbf{A}|^\top\mathbf{L}\right)^\top \mathbf{1} \tag{51a}$$

$$\left(\mathbf{A}^\top\mathbf{H} + \frac{1}{2}|\mathbf{A}|^\top\mathbf{K}\right)^\top \check{\mathbf{K}}^\top = \left(\mathbf{A}^\top\mathbf{H} + \frac{1}{2}|\mathbf{A}|^\top\mathbf{K}\right)^\top \mathbf{1} \tag{51b}$$

B Lazy Constraint Algorithm

Figure 3 shows the lazy algorithm implemented for the distribution factor OPF models. Let $\mathcal{K}^{\text{mon}}$ and $\mathcal{N}^{\text{mon}}$ be input data for the initial set of constraints (16), (17), and (26) that are explicitly included in the model formulation. Then, each iteration solves the OPF model and determines if any of the excluded constraints have been violated and adds them to the monitored set. Because the algorithm terminates only after all constraints have been satisfied, the resulting solution is both feasible and optimal in the extensive formulation.

A similar algorithm is not presented for the S-LOPF. The S-LOPF's formulation consists of $K + N$ power flow and power balance constraints and $K + N$ power flow and voltage variables, for both real and reactive power, that must be simultaneously satisfied. Dropping any of the power flow constraints could therefore cause the power flow and voltage variables to violate Kirchhoff's laws.

The algorithm in Figure 3 was implemented in Python using the Pyomo algebraic modeling language [5, 6]. Pyomo's persistent interface to the Gurobi solver [7] was used to take advantage of LP warm-starting. The algorithm is also implemented for the P-LOPF and PTDF model formulations by dropping lines 6, 7, and 9, as well as the sets $\mathcal{N}^{\text{mon}}$ and $\mathcal{N}^{\text{vio}}$ and the output variable $\mathbf{q}^{\mathbf{nw}*}$. Branch constraints were added to the initial monitored set if the apparent

[2] The calculation for $\check{\mathbf{L}}$ requires the same reference bus modification previously noted for $\hat{\mathbf{F}}$ and $\hat{\mathbf{L}}$.

power flows the base-point solution were within 25% of the limit, and bus voltage constraints were added if the voltage magnitude in the base-point solution was within 15% of either the upper or lower limit. A maximum of 50 violated thermal constraints and 50 violated voltage magnitude constraints were added per iteration. A more efficient future implementation could use the implied constraint satisfaction technique by [8] to further reduce the number of added constraints by selecting the added constraints in a more intelligent fashion.

C Computational Results

Table 2 shows the full suite of test cases in which the solutions to the LOPF models were attempted. All cases are sourced from [11] and reflect typical operating conditions.

C.1 Objective Function Error

Objective function values for each test case are shown in Table 3, where each objective function has been normalized by the locally optimal AC OPF solution, resulting in a unitless quantity. The LOPF models are approximations rather than relaxations of the AC OPF, and therefore their optimal objective function may be higher or lower than the optimal AC OPF objective. Nevertheless, most of the LOPF models fall within 1% of the AC OPF objective. Exceptions to this include: case300_ieee,[3] case162_ieee_dtc,[4] case1888_rte, case6495_rte, and case6515_rte.

C.2 LMP Error

LMPs help to provide an economic signal that indicates how much power should be produced at each location in the power network. For example, if there is a binding transmission constraint, then resources that reduce flow on the constraint (i.e., $\hat{F}_{ik} < 0$ for node i and binding constraint k) would receive a higher energy price than resources whose production would increase the flow on the constraint (i.e., $\hat{F}_{ik} > 0$ for node i and binding constraint k). The following section compares the LMPs determined from the LOPF, PTDF and B-theta models to see how well each model is able to identify the same constraints and determine similar prices as the AC OPF.

A few caveats about LMP accuracy should first be noted. OPF formulation improvements are intended to determine more efficient dispatch by improving the physical modeling of the system. In contrast, LMPs are an economic signal that may have no objectively true value to compare against. When an OPF model (such as the LOPF, PTDF, or B-theta) uses approximated power flows, the dispatch solution may differ slightly from the AC OPF solution, and therefore the resulting LMPs could change significantly although the dispatch is still

[3] The solution to case300_ieee is known to have unrealistic phase angle differences.

[4] case162_ieee_dtc is intended for dynamic case studies.

very close to the actual optimal solution. Nonetheless, the following LMP results indicate that the models tend to correctly identify and price the system's binding constraints fairly consistently with the AC OPF.

Figure 4 shows a heatmap of LMPs in the IEEE 118-bus test case. The figure shows the higher fidelity of the S/D/C/P-LOPF models compared to the PTDF and B-theta models. These DC OPF implementations correctly identify changes in LMP due to congestion but not due to line losses in the network, so the LMP heatmap for these simplified models appears "blurry" compared to the other models with more accurate approximations, especially the effect of line loading on higher line losses. LMPs from the S/D/C/P-LOPF models are almost identical to those from the AC OPF.

Although the LOPF approximations tend to be more accurate than the PTDF and B-theta models, higher accuracy is not necessarily guaranteed.[5] Figure 5 displays LMP heatmaps of four of the Polish test cases compared to the AC OPF solution's LMPs. The cases respectively represent network and demand conditions in winter peak (Figure 5a), winter off-peak (Figure 5b), summer peak (Figure 5c), and summer off-peak (Figure 5d) periods. Figures 5a and 5c include price spikes that exceed $250/MWh at some nodes, indicated by the white areas of the heatmap. A few notes on these results are detailed below.

First, Figure 5a illustrates an important difficulty in assessing the quality of OPF solutions. The diagram shows that the PTDF and B-theta models both correctly identify the location of the highest LMP nodes and visually provide better matches to the AC OPF's LMPs than the S/D/C-LOPF models. However, because each OPF solution may differ from the AC OPF base-point, the change in LMPs does not necessarily indicate a worse solution. According to Table 3, the solutions from the PTDF and B-theta models are about 1% more expensive than the AC OPF solution. A more detailed look at the prices also shows that highest LMPs in the DC OPF solutions are substantially higher than in the AC OPF solution ($957.52/MWh in the PTDF, $887.48/MWh in B-theta, and $634.83/MWh in the AC OPF). That is, the PTDF and B-theta models have determined a more expensive dispatch solution, and the additional dispatch costs are also reflected in higher LMPs. In contrast, Table 3 shows that the S/D/C-LOPF models are about 0.2% below the optimal objective cost. The S/D/C-LOPF models indeed violated a handful of thermal constraints in the subsequent AC power flow, but the violations are very small (4.0, 4.0, and 3.8 MVAr on a branch with 250 MVAr capacity). In the AC power flow solutions, the PTDF and B-theta generator dispatch resulted in constraint violations of 51.0 and 53.9 MVAr on a branch with 400 MVAr capacity. The P-LOPF model also resulted in a 34.4 MVAr constraint violation on the same 400 MVAr branch, even though its LMPs match closely with the AC OPF solution and its objective function is accurate to 0.01%. In other words, highly accurate LMP results in Figure 5a do not necessarily correspond to higher quality OPF solutions since remedial actions may be needed to resolve constraint violations that were not

[5] In other words, the approximations cannot be said to be "stronger" in the same sense that some AC OPF relaxations are stronger than others [25].

modeled accurately.

Figures 5b and 5d show similar results as Figure 4, with the LOPF models providing a higher fidelity model of the network and therefore more accurate LMPs. Lastly, Figure 5c shows similar results as explained for Figure 5a. As was the case for case2383wp_k, the LOPF solutions in case3120sp_k also appear to be less accurate than for the DC OPF solutions. However, closer examination also reveals that the LOPF solutions only resulted in small constraint violations in the AC power flow. In comparison, the PTDF and B-theta models correctly identify the problematic constraints, but the constraints have comparatively large violations in the AC power flow because the PTDF and B-theta approximations are not as accurate as those in the LOPF models. Note, however, that the PTDF and B-theta models are "flat start" DC OPF implementations that are not typically used in the OPF software used by ISOs.

C.3 Power Flow Error

An AC power flow was solved after finding each optimal solution to assess power flow errors. The AC power flow is implemented in the standard fashion [26] by fixing the real power output and voltage magnitude at each generator (PV) bus, fixing real and reactive power demand at each load (PQ) bus, and fixing voltage angle and magnitude at the slack, or reference, bus.

Figure 6 shows the 50 largest real power flow errors in the each of the four Polish test cases: winter peak (Figure 6a), winter off-peak (Figure 6b), summer peak (Figure 6c), and summer off-peak (Figure 6d). The proposed S/D/C-LOPF models result in very little power flow error while the B-theta and PTDF models show significant power flow error. In each test case, the largest power flow errors occur at the branches connected to the reference bus since it provides the additional power injections to resolve power flow infeasibilities. Power flows in the S/D/C/P-LOPF models are nearly feasible, therefore requiring less power from the reference bus and resulting in less power flow error.

Figure 7 summarizes the real power flow errors in terms of the median, mean, and maximum absolute errors. Note that the y-axis is shown in log scale. In some cases, such as in Figures 7a and 7b, real power flow errors are actually lower in the C-LOPF than for the larger S-LOPF and D-LOPF models. This underscores that the C-LOPF's simplifications maintain a very high degree of consistency with the underlying AC power flow physics. From the plots, it can also be seen that the C-LOPF shows a higher degree of accuracy than the P-LOPF even though the two formulations only differ in that the C-LOPF's reactive power and voltage constraints are dropped in the P-LOPF formulation. Since the real power constraints are the same in both models, it may be surprising that the two would result in different power flow error. This highlights the benefits of modeling reactive power in OPF formulations; the C-LOPF is able to provide generator voltage set points, $\mathbf{v}^*$, that are more consistent with each generator's real power dispatch.

C.4 Simplification Results

Simplification techniques that are common in practice often do not appear to be very effective when implemented on the standard set of IEEE test cases because the test cases are too small to show improvements. Figure 8 compares solution times with and without applying the "lazy" algorithm in the IEEE cases (Figure 8a) and Polish test cases (Figure 8b). Figure 8a shows that the lazy algorithm actually increases solution times in the smaller IEEE cases. However, Figure 8 shows substantial speed improvements in the set of larger Polish test cases that are noted in [1]. These results are consistent with common ISO practices and demonstrate that the lazy algorithm's effectiveness is case dependent and tends to be most favorable in larger test cases.

Three relative tolerance levels ε^{rel} were also tested, $10^{-6}, 10^{-4}$, and 10^{-2}, denoted by "full," "e4," and "e2," respectively, in Figure 9. Like for the lazy algorithm, the factor truncation procedure is based on common ISO practices. In Figure 9a, the truncation procedure can be seen to improve the worst-case solution times in the IEEE test cases, but has no significant effect on average or median solution times. Figure 9b shows results from the larger Polish test cases, and the truncation procedure provides a very clear reduction in the median and worst-case solution times, such that there is almost no overlap between the box plots with the smallest (full) and largest (e2) truncation tolerances. Again, the effectiveness of this simplification technique may only be apparent in larger test cases.

However, factor truncation can distort power flows. Figure 10 shows the effect of the factor truncation procedure on power flow distortions in the D- and C-LOPF models. As shown in the figure, only the "e2" truncation threshold results in any significant error. However, the errors are much smaller than the power flow errors of the P-LOPF model, and especially smaller than the power flow errors of the B-theta and PTDF models.

Finally, Figures 6 and 10 also provide confirmation that the hybrid line loss constraints described in Section II-E does not result in significant power flow errors. In each Polish test case, the D-LOPF is implemented with hybrid line loss constraints, and there is no noticeable increase in power flow error compared to the S-LOPF errors.

C.5 Varying the Demand Levels

Although the above results indicate that the LOPF models perform well when the system conditions are identical to the base-point solution, it is also important to assess how sensitive the model's accuracy is to changes in system demand [27]. Although power flow accuracy is case dependent and is therefore affected by changes in demand, the following results show that the change tends to be small and within the same error as in the results with nominal demand.

The sensitivity analysis was performed by varying demand levels $\mathbf{P^d}$ by a multiplicative factor. This multiplier was initialized at 0.95 and increased to 1.05 in 0.01 increments. Then, each LOPF model was solved at each demand

using the sensitivity factors calculated from the base-point solution (i.e., where the multiplier equals one). To prevent infeasible model instances, a screening step was performed which narrowed the range of the demand multiplier (and decreased the increment size) as needed to ensure that feasible AC OPF solutions can be obtained at each demand level. A nominal demand multiplier equal to one was always included, bringing the maximum number of problem instances to 12.

Figure 11 shows the sensitivity results for the IEEE 118-bus test case. In Figure 11a, the total costs in each sensitivity remain well within 1% of the AC OPF cost. The reference bus slack shown in Figure 11b and power flow errors in Figures 11c and 11d also stay within a close range of the error levels as the nominal demand case.

Power flow errors are vector-valued, so they are summarized by the 1-norm and ∞-norm. By definition, the 1-norm is equivalent to a sum of the absolute power flow errors, and the ∞-norm is equivalent to the maximum absolute error. The general p-norm is denoted $\|\cdot\|_p$ and is defined for $p \geq 1$ as:

$$\|\mathbf{x}\|_p := \left(\sum_k |x_i|^p \right)^{(1/p)}$$

Figure 12 summarizes the error sensitivities of other IEEE test cases, excluding case300 because it is known to include unrealistically large phase angle differences. The remaining cases in the IEEE set all display less error than the 118-bus test case. Errors of the S/D/C-LOPF models are almost identical and are generally lower than for the P-LOPF model that does not include reactive power and voltage constraints. Additional sensitivity analyses are not included for the other test case sets due to the memory and computational time required to execute the larger test cases.

C.6 Solution Times

Figure 13 displays the solution times of each model formulation variation and each set of test cases. The proposed model formulations tended to show the largest effect on solution times in larger ($> 1,000$-bus) test cases, especially the Polish cases in Figure 13e. In contrast, it is difficult to discern any significant solution time reduction in sets with smaller test cases like IEEE (Figure 13b) and MISC (Fig. 13f), and as previously mentioned, the lazy algorithm appears to increase solution times in the small cases even though it reduces solution times in the larger cases. These smaller test cases are often used to demonstrate new OPF solution algorithms, yet our results suggest that small ($< 1,000$-bus) test cases are almost useless for assessing the performance of OPF algorithms and simplifications.

Lastly, Table 4 displays the solution speedup of different model implementations compared to the AC OPF. Speedup is defined as the geometric mean of the AC OPF solution times divided by the geometric mean of the specific model's solution times, so a speedup >1 implies that the model solved faster than the

AC OPF on average. Geometric means are used so that the model rankings are invariant to which model is used to define the baseline (i.e., AC OPF) and to reduce the influence of outliers. Any cases that were not solved by all models are excluded from the mean data. Default model implementations are marked "D" (for default) and the implementations with the lazy algorithm and a relative factor truncation tolerance of 10^{-2} is marked "LT" (for lazy/truncation). The default PTDF implementation actually outperforms the B-theta models yet runs significantly slower with the LT implementation settings. However, general conclusions avoided since the paper omits detailed explanations of the PTDF and B-theta implementations. The P-LOPF almost always has higher speedup than the S-LOPF, and the S-LOPF generally has higher speedup than the D/C-LOPF models.

Relative performance of each model is also highly case dependent. For example, the S-LOPF's speedup is higher in the SDET cases than the Polish cases, yet the C-LOPF's LT implementation has higher speedup in the Polish cases than in the RTE cases. Part of the reasoning for this, as previously alluded to in Section III-C, is that the efficacy of the LT simplifications for the D/C-LOPF's depends on the size of the test case. Accordingly, the LT implementation only provides a D-LOPF speedup benefit in the Polish, RTE, TAMU, and MISC test cases, and it provides a C-LOPF speedup benefit in the Polish, SDET, and RTE test cases.

Solution speeds in specific test cases is therefore nontrivial and should be thoroughly investigated for each potential real-world application individually. For example, the sparse formulation of the S-LOPF often outperforms the C-LOPF in small OPF test cases, but the compact formulation of the C-LOPF may have benefits in larger test cases or when embedded in more complex security-constrained or UC problems.

Acknowledgment

The research in this article was supported by the U.S. Department of Energy's Office of Electricity through the Advanced Grid Modeling program under project title "Reassessing the Market—Computation Interface to Enhance Grid Security and Efficiency."

References

[1] B. Eldridge, A. Castillo, B. Knueven, and M. Garcia, "Sparse, dense, and compact linearizations of the AC OPF," 2020.

[2] M. Garcia, R. Baldick, and S. Siddiqi, "A general economic dispatch problem with marginal losses," in *2019 American Control Conference (ACC)*. IEEE, 2019, pp. 2588–2595.

[3] B. Stott and O. Alsac, "Fast decoupled load flow," *IEEE Transactions on Power Apparatus and Systems*, vol. PAS-93, no. 3, pp. 859–869, 1974.

[4] D. G. Luenberger and Y. Ye, "Linear and nonlinear programming," 2008.

[5] W. E. Hart, J. P. Watson, and D. L. Woodruff, "Pyomo: Modeling and solving mathematical programs in Python," *Mathematical Programming Computation*, vol. 3, no. 3, pp. 219–260, 2011.

[6] W. E. Hart, C. D. Laird, J. P. Watson, D. L. Woodruff, G. A. Hackebeil, B. L. Nicholson, and J. D. Siirola, *Pyomo–optimization modeling in Python*, 2nd ed. Springer Science & Business Media, 2017, vol. 67.

[7] Gurobi Optimization, LLC, "Gurobi optimizer reference manual," 2020. [Online]. Available: http://www.gurobi.com

[8] L. A. Roald and D. K. Molzahn, "Implied constraint satisfaction in power system optimization: The impacts of load variations," in *2019 57th Annual Allerton Conference on Communication, Control, and Computing (Allerton)*. IEEE, 2019, pp. 308–315.

[9] D. Kincaid, D. R. Kincaid, and E. W. Cheney, *Numerical analysis: Mathematics of scientific computing*. American Mathematical Soc., 2009, vol. 2.

[10] B. Knueven, C. Laird, J. P. Watson, M. Bynum, A. Castillo, and USDOE, "Egret v. 0.1 (beta), version v. 0.1 (beta)," 3 2019. [Online]. Available: https://www.osti.gov//servlets/purl/1498854

[11] S. Babaeinejadsarookolaee, A. Birchfield, R. D. Christie, C. Coffrin, C. DeMarco, R. Diao, M. Ferris, S. Fliscounakis, S. Greene, R. Huang *et al.*, "The power grid library for benchmarking AC optimal power flow algorithms," *arXiv preprint arXiv:1908.02788*, 2019.

[12] *Power systems test case archive*, University of Washington, 1999, http://www2.ee.washington.edu/research/pstca.

[13] *Sustainable Data Evolution Technology (SDET)*, Pacific Nortwest National Laboratory (PNNL), March 2018, https://egriddata.org/group/sustainable-data-evolution-technology-sdet.

[14] C. Josz, S. Fliscounakis, J. Maeght, and P. Panciatici, "AC power flow data in MATPOWER and QCQP format: iTesla, RTE snapshots, and PEGASE," *arXiv preprint arXiv:1603.01533*, 2016.

[15] A. B. Birchfield, T. Xu, K. M. Gegner, K. S. Shetye, and T. J. Overbye, "Grid structural characteristics as validation criteria for synthetic networks," *IEEE Transactions on Power Systems*, vol. 32, no. 4, pp. 3258–3265, 2016.

[16] R. D. Zimmerman, C. E. Murillo-Sánchez, and R. J. Thomas, "MATPOWER: Steady-state operations, planning and analysis tools for power systems research and education," *IEEE Transactions on Power Systems*, vol. 26, no. 1, pp. 12–19, 2011.

[17] B. C. Lesieutre, D. K. Molzahn, A. R. Borden, and C. L. DeMarco, "Examining the limits of the application of semidefinite programming to power flow problems," in *2011 49th annual Allerton conference on communication, control, and computing (Allerton)*. IEEE, 2011, pp. 1492–1499.

[18] F. Li and R. Bo, "Small test systems for power system economic studies," in *IEEE PES General Meeting*. IEEE, 2010, pp. 1–4.

[19] P. F. Albrecht, M. P. Bhavaraju, B. E. Biggerstaff, R. Billinton *et al.*, "IEEE reliability test system: A report prepared by the reliability test system task force of the application of probability methods subcommittee," *IEEE Transactions on Power Apparatus and Systems*, vol. 98, no. 6, pp. 2047–2054, 1979.

[20] O. Alsac and B. Stott, "Optimal load flow with steady-state security," *IEEE Transactions on Power Apparatus and Systems*, vol. PAS-93, no. 3, pp. 745–751, 1974.

[21] M. A. Pai, *Energy function analysis for power system stability*. Springer Science & Business Media, 2012.

[22] C. Grigg, P. Wong, P. Albrecht, R. Allan, M. Bhavaraju, R. Billinton, Q. Chen, C. Fong, S. Haddad, S. Kuruganty *et al.*, "The IEEE reliability test system-1996. a report prepared by the reliability test system task force of the application of probability methods subcommittee," *IEEE Transactions Power Systems*, vol. 14, no. 3, pp. 1010–1020, 1999.

[23] M. Szechtman, L. Pilotto, W. Ping, E. Salgado, A. Dias de Carvalho, W. Long, F. Alvarado, C. DeMarco, C. Canizares, and A. Wey, "Dc multi-infeed study. final report," Electric Power Research Institute (EPRI, Tech. Rep. EPRI-TR-104586, 12 1994.

[24] J. E. Price and J. Goodin, "Reduced network modeling of WECC as a market design prototype," in *2011 IEEE Power and Energy Society General Meeting*. IEEE, 2011, pp. 1–6.

[25] D. K. Molzahn and I. A. Hiskens, *A survey of relaxations and approximations of the power flow equations*. Now Publishers, 2019.

[26] J. D. Glover, M. Sarma S, and T. J. Overbye, *Power systems analysis and design*, 4th ed. Thompson Learning, 2008.

[27] R. Baldick, K. Dixit, and T. J. Oberbye, "Empirical analysis of the variation of distribution factors with loading," in *IEEE Power Engineering Society General Meeting, 2005*. IEEE, 2005, pp. 221–229.

Table 2: OPF case study sources

Source:	IEEE[a]	SDET[b]	PEGASE[c]	TAMU[d]
Cases:	case14_ieee	case588_sdet	case89_pegase	case200_tamu
	case30_ieee	case2316_sdet	case1354_pegase	case500_tamu
	case57_ieee	case2853_sdet	case2869_pegase	case2000_tamu
	case118_ieee	case4661_sdet	case9241_pegase	case10000_tamu
	case300_ieee		case13659_pegase	
Source:	Polish[e]	RTE[c]	MISC	
Cases:	case2383wp_k	case1888_rte	case3_lmbd[f]	
	case2736sp_k	case1951_rte	case5_pjm[g]	
	case2737sop_k	case2848_rte	case24_ieee_rts[h]	
	case2746wop_k	case2868_rte	case30_as[i]	
	case2746wp_k	case6468_rte	case30_fsr[i]	
	case3012wp_k	case6470_rte	case39_epri[j]	
	case3120sp_k	case6495_rte	case73_ieee_rts[k]	
	case3375wp_k	case6515_rte	case162_ieee_dtc[l]	
			case179_goc[m]	
			case240_pserc[n]	

[a] IEEE Power Flow Test Cases [12]
[b] Sustainable Data Evolution Technology (SDET) Test Cases [13]
[c] Pan European Grid Advanced Simulation and State Estimation (PEGASE) and Réseau de Transport d'Électricité (RTE) Test Cases [14]
[d] Texas A & M University (TAMU) Test Cases [15]
[e] Polish Test Cases [16]
[f] 3-Bus test Case [17]
[g] 5-Bus PJM Test Case [18]
[h] RTS-79 [19]
[i] 30 Bus-as and 30 Bus-fsr [20]
[j] Case39 [21]
[k] RTS-96 [22]
[l] 17 Generator IEEE Dynamic Test Case [12]
[m] 179 Bus Grid Optimization Competition Test Cases [23]
[n] WECC 240 Bus Power Systems Engineering Research Center (PSERC) Test Case [24]

Table 3: Normalized objective function values, default model implementations

Case	S-LOPF	D-LOPF	C-LOPF	P-LOPF	PTDF	B-theta
case14_ieee	1.000	1.000	1.000	1.000	1.000	1.000
case30_ieee	1.000	1.000	1.000	0.992	0.997	1.001
case57_ieee	0.999	0.999	0.999	0.999	0.970	0.969
case118_ieee	0.999	0.999	0.999	0.999	0.996	0.998
case300_ieee	0.956	0.957	0.950	0.957	0.943	0.943
case2383wp_k	0.998	0.998	0.998	1.000	1.013	1.009
case2736sp_k	1.000	1.000	1.000	1.000	1.000	1.000
case2737sop_k	1.000	1.000	1.000	1.000	1.000	1.000
case2746wop_k	1.000	1.000	1.000	1.000	1.000	1.000
case2746wp_k	1.000	1.000	1.000	1.000	1.000	1.000
case3012wp_k	0.999	0.999	0.999	1.000	0.998	1.000
case3120sp_k	1.000	1.000	1.000	1.000	1.000	1.001
case3375wp_k	1.000	1.000	1.000*	1.000	1.000	1.000
case588_sdet	1.000	1.000	1.000	1.000	1.001	1.002
case2316_sdet	1.000	1.000	1.000	1.000	1.006	1.001
case2853_sdet	1.000	1.000	1.000	0.999	1.000	1.002
case4661_sdet	0.999	0.999*	0.999*	1.000	1.002	1.001
case1888_rte	0.978	0.978	0.978	0.979	0.986	0.986
case1951_rte	1.000	1.000	1.000	1.000	1.000	1.000
case2848_rte	1.000	1.000	1.000	1.000	0.999	0.999
case2868_rte	1.000	1.000	1.000	1.000	1.000	1.000
case6468_rte	1.000	****	****	1.000	1.000*	1.002
case6470_rte	0.999	****	****	1.000	1.006*	1.006
case6495_rte	0.939	****	****	1.017	0.882*	0.971
case6515_rte	0.983	****	****	1.003	0.959*	1.002
case89_pegase	0.999	0.999	0.999	0.998	1.000	***
case1354_pegase	0.999	0.999	0.999	0.992	0.998	1.000
case2869_pegase	1.000	1.000	1.000	0.999	1.000	0.998
case9241_pegase	1.000	****	****	****	****	****
case13659_pegase	1.000	****	****	****	****	****
case200_tamu	1.000	1.000	1.000	1.000	1.000	1.000
case500_tamu	0.999	0.999	0.999	1.000	0.999	1.002
case2000_tamu	1.000	1.000	1.000	1.000	1.017	0.999
case10000_tamu	1.000	****	****	1.000**	****	****
case3_lmbd	0.990	0.990	0.990	0.999	0.999	0.999
case5_pjm	0.997	0.997	0.997	0.997	1.006	1.006
case24_ieee_rts	1.000	1.000	1.000	1.000	1.000	1.000
case30_as	1.000	1.000	1.000	1.000	0.997	0.997
case30_fsr	0.999	0.999	0.999	1.000	0.999	0.999
case39_epri	0.998	0.998	0.998	1.000	0.998	0.998
case73_ieee_rts	1.000	1.000	1.000	1.000	1.000	1.000
case162_ieee_dtc	0.974	0.974	0.974	0.990	0.974	0.987
case179_goc	1.000	1.000	1.000	1.000	1.000	1.000
case240_pserc	0.995	0.995	0.995	0.996	1.000	1.000

* Lazy model, default parameter tolerances
** Lazy model, 10^{-2} relative parameter tolerances
*** Infeasible
**** Memory crash

Table 4: Model speedup compared to AC OPF, by implementation settings

Model	S-LOPF	D-LOPF		C-LOPF		P-LOPF		PTDF		B-theta
Implementation	D	D	LT	D	LT	D	LT	D	LT	D
IEEE	29.9	22.4	11.7	28.2	13.4	90.7	18.1	244.6	10.8	87.5
Polish	9.4	2.1	4.7	3.7	8.5	18.2	37.0	95.5	31.4	24.2
SDET	16.2	3.2	3.1	4.8	5.4	30.4	6.6	96.5	2.0	60.9
RTE	60.9	2.5	13.6	13.1	29.1	37.4	42.8	444.1	39.0	136.7
PEGASE	9.1	2.1	2.0	4.1	4.0	11.9	12.0	75.1	5.3	61.8
TAMU	22.2	3.5	6.9	5.2	3.9	46.3	70.7	275.7	17.5	120.6
MISC	23.2	8.5	12.3	20.2	15.3	43.0	15.5	86.5	11.6	64.2

Figure 3: Lazy constraint algorithm for the D-LOPF and C-LOPF models

Input: D-LOPF or C-LOPF model, initial monitored sets $\mathcal{K}^{\text{mon}}, \mathcal{N}^{\text{mon}}$

$\mathcal{K}^{\text{vio}} = \mathcal{N}^{\text{vio}} = \varnothing$

repeat

  $\mathcal{K}^{\text{mon}} = \mathcal{K}^{\text{mon}} \cup \mathcal{K}^{\text{vio}}$, and $\mathcal{N}^{\text{mon}} = \mathcal{N}^{\text{mon}} \cup \mathcal{N}^{\text{vio}}$

  Solve LOPF with monitored constraints $\mathcal{K}^{\text{mon}}$ and $\mathcal{N}^{\text{mon}}$

  $\mathbf{p}^{\mathbf{f}\alpha} = \hat{\mathbf{F}}\mathbf{p}^{\mathbf{nw}*} + \mathbf{F}^{\mathbf{0}}$

  $\mathbf{q}^{\mathbf{f}\alpha} = \hat{\mathbf{H}}\mathbf{q}^{\mathbf{nw}*} + \mathbf{H}^{\mathbf{0}}$

  $\mathbf{v} = \hat{\mathbf{S}}_{\mathbf{v}}\mathbf{q}^{\mathbf{nw}*} + \mathbf{S}_{\mathbf{v}}^{\mathbf{0}}$

  $\mathcal{K}^{\text{vio}} = \{k \in \mathcal{K} \text{ such that } (p_k^{f\alpha})^2 + (q_k^{f\alpha})^2 > \overline{T}_k^2\}$

  $\mathcal{N}^{\text{vio}} = \{k \in \mathcal{N} \text{ such that } v_n < \underline{V}_n \text{ or } v_n > \overline{V}_n\}$

until $\mathcal{K}^{\text{vio}} \subset \mathcal{K}^{\text{mon}}$ **and** $\mathcal{N}^{\text{vio}} \subset \mathcal{N}^{\text{mon}}$

Output: $\mathbf{p}^{\mathbf{nw}*}, \mathbf{q}^{\mathbf{nw}*}$

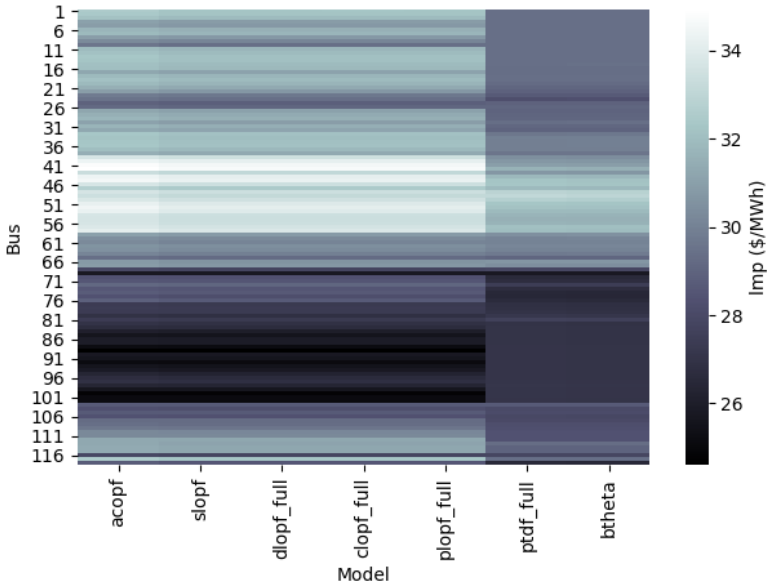

Figure 4: LMP comparison in the 118-bus IEEE test case with nominal demand.

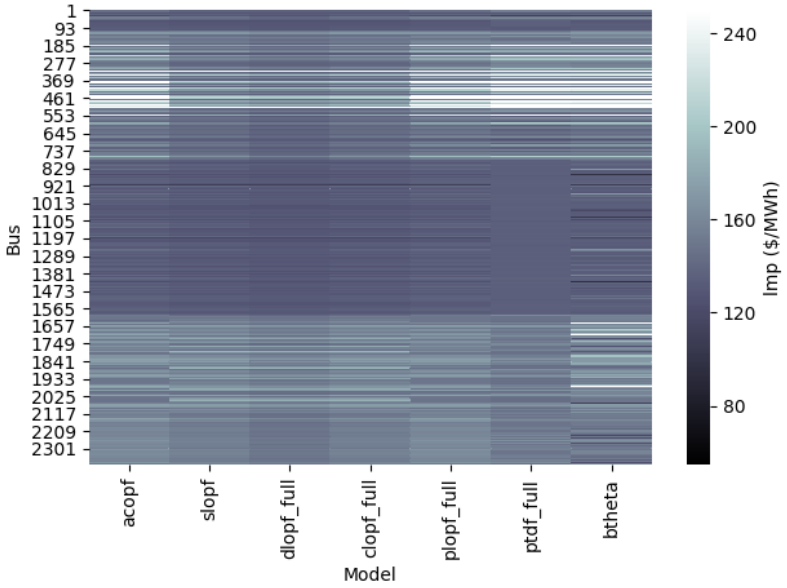

(a) case2383wp_k

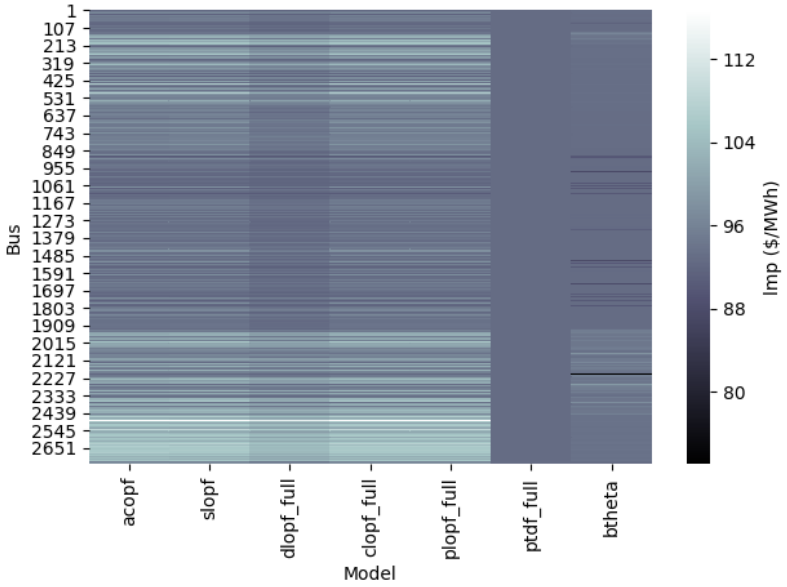

(b) case2746wop_k

Figure 5: LMP errors in Polish test cases with nominal demand.

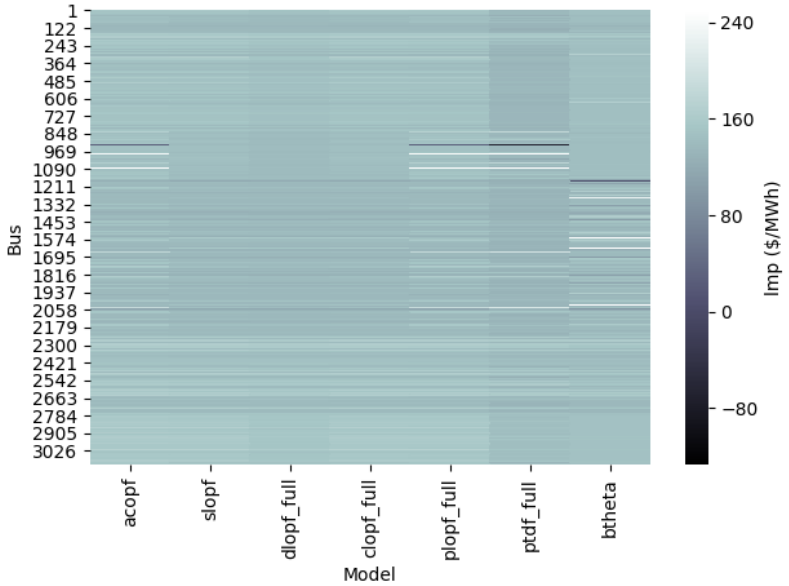

(c) case3120sp_k

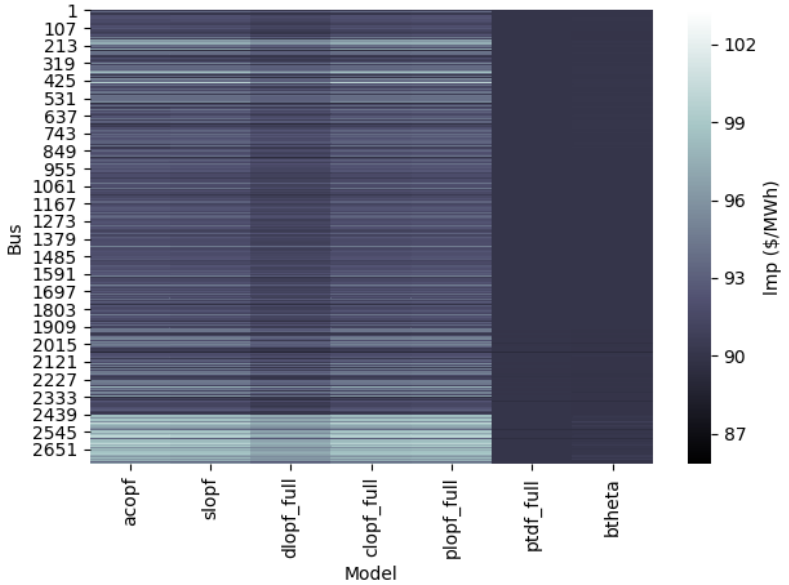

(d) case2737sop_k

Figure 5: LMP errors in Polish test cases with nominal demand.

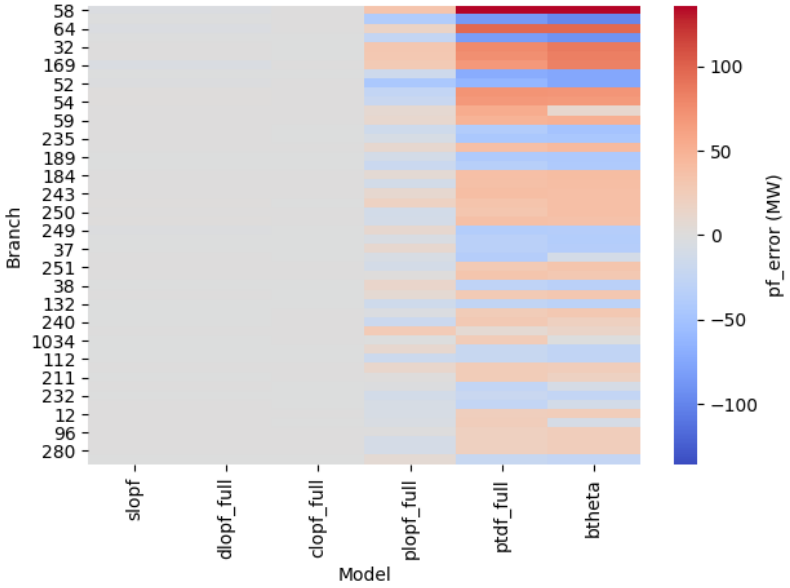

(a) case2383wp_k

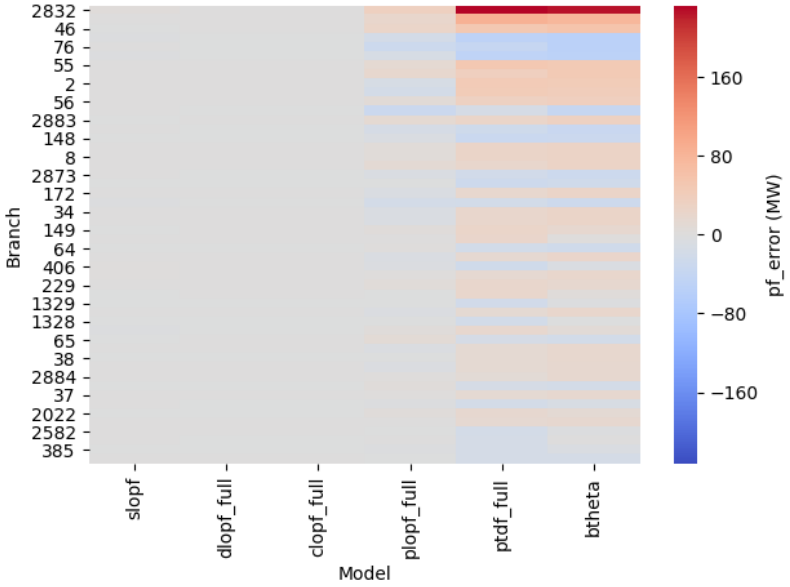

(b) case2746wop_k

Figure 6: Real power flow errors in Polish test cases with nominal demand.

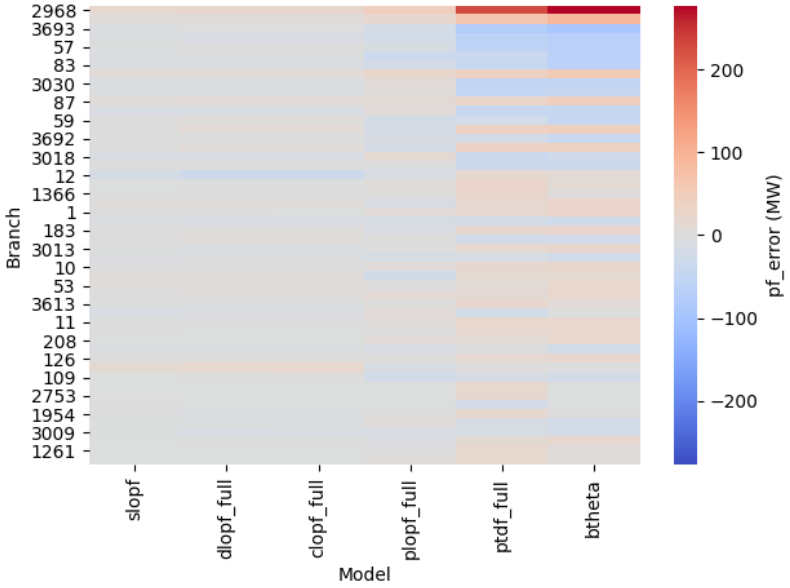

(c) case3120sp_k

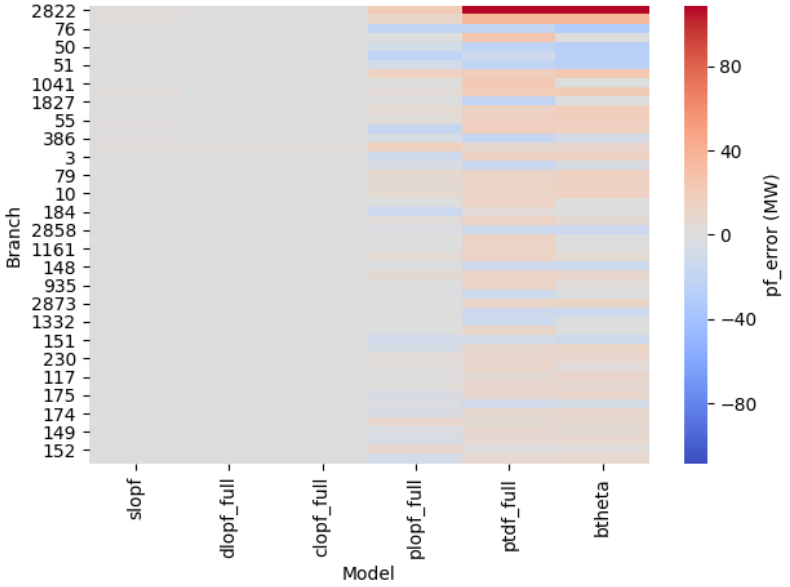

(d) case2737sop_k

Figure 6: Real power flow errors in Polish test cases with nominal demand.

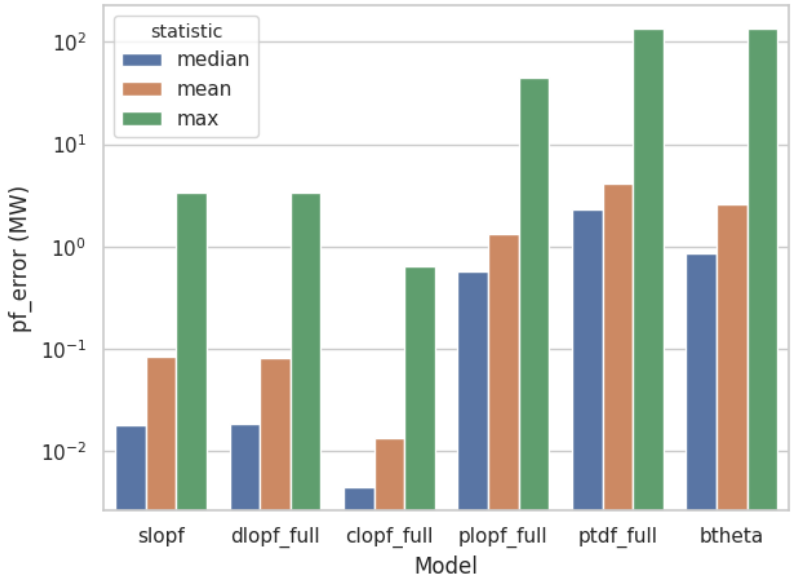

(a) case2383wp_k

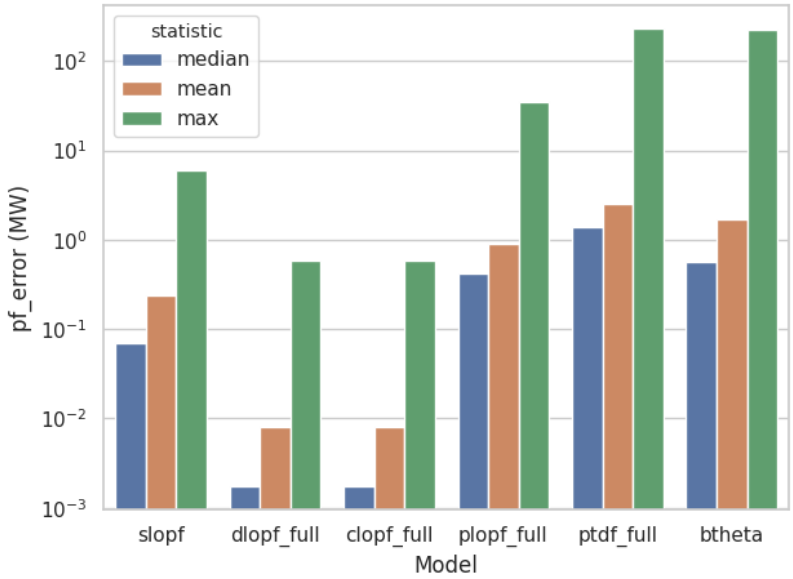

(b) case2746wop_k

Figure 7: Real power flow error statistics in Polish test cases with nominal demand.

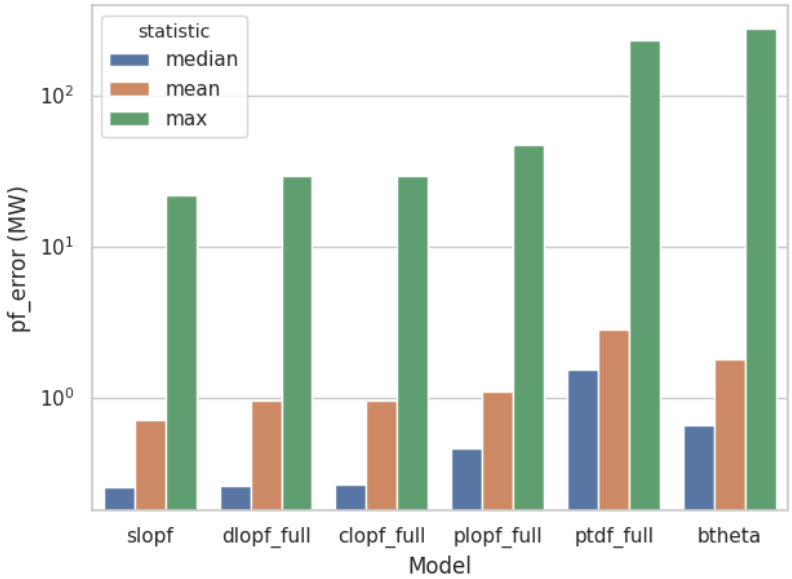

(c) case3120sp_k

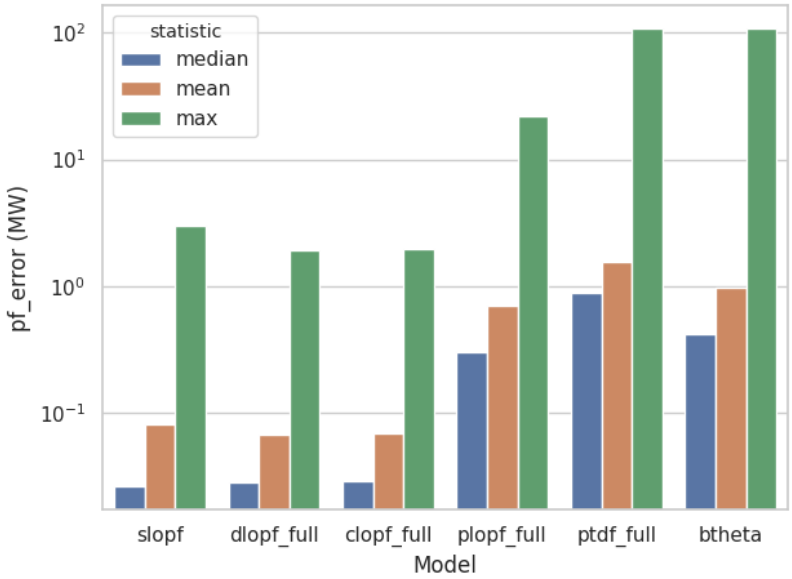

(d) case2737sop_k

Figure 7: Real power flow error statistics in Polish test cases with nominal demand.

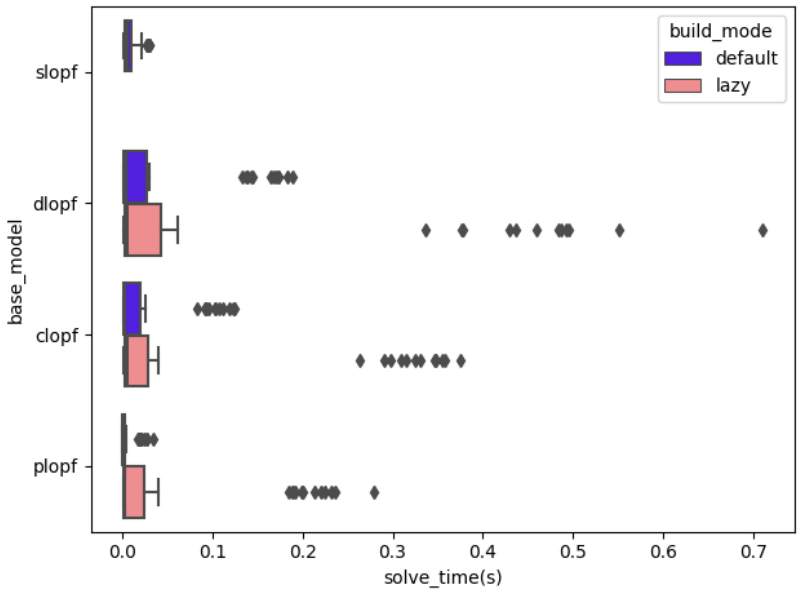

(a) IEEE cases

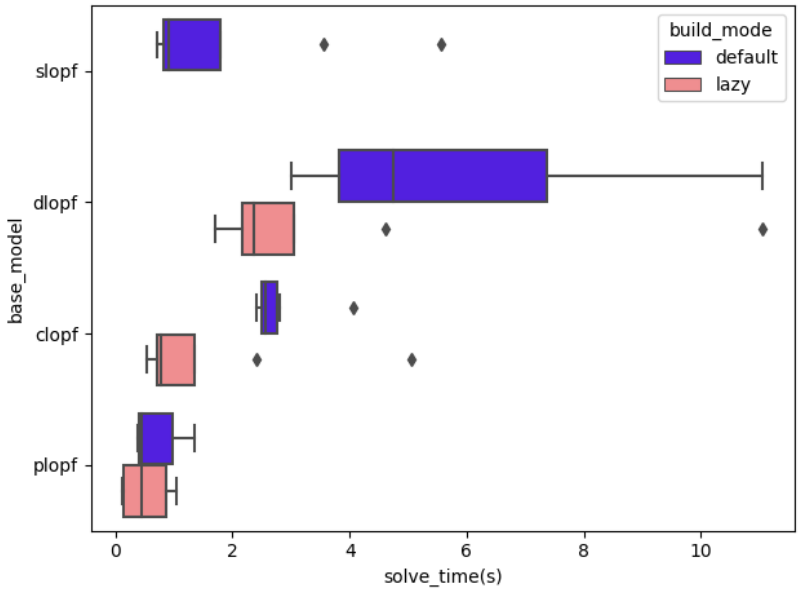

(b) Polish cases

Figure 8: Solution times in IEEE and Polish test cases with and without lazy algorithm.

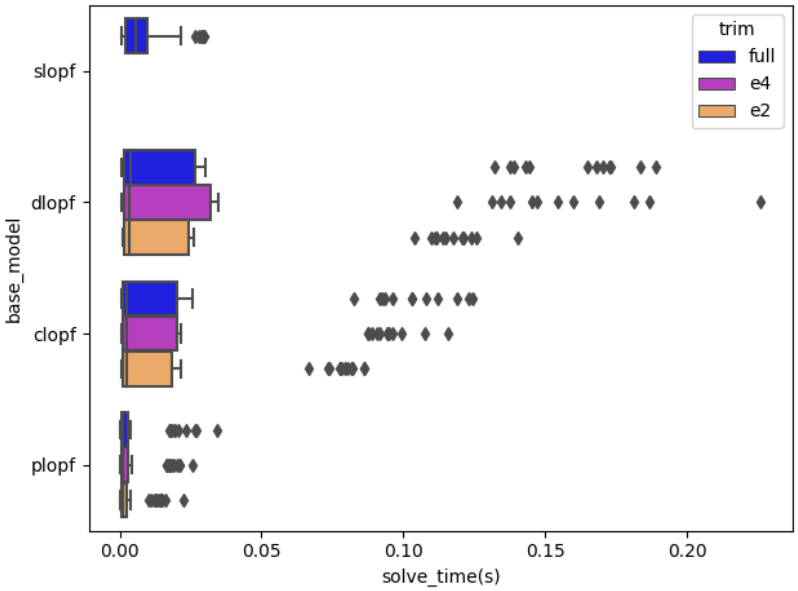

(a) IEEE cases

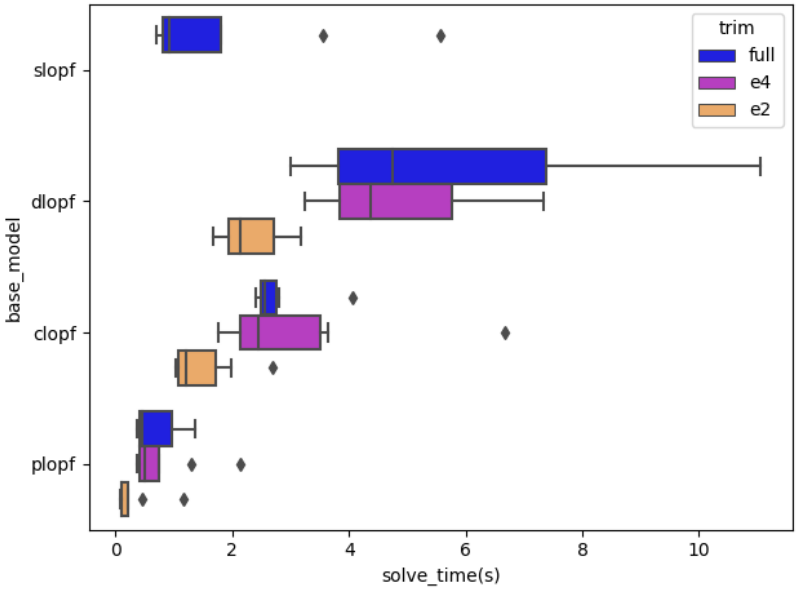

(b) Polish cases

Figure 9: Solution times in IEEE and Polish test cases with factor truncation tolerances.

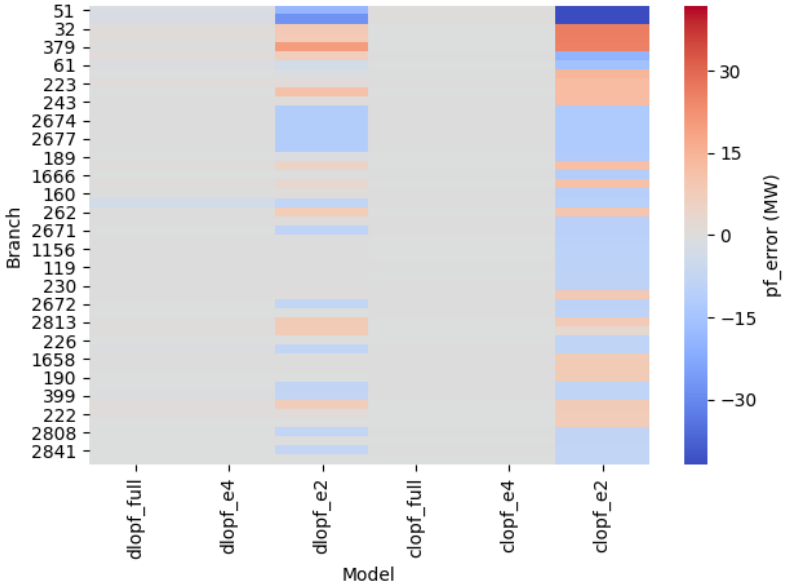

(a) case2383wp_k

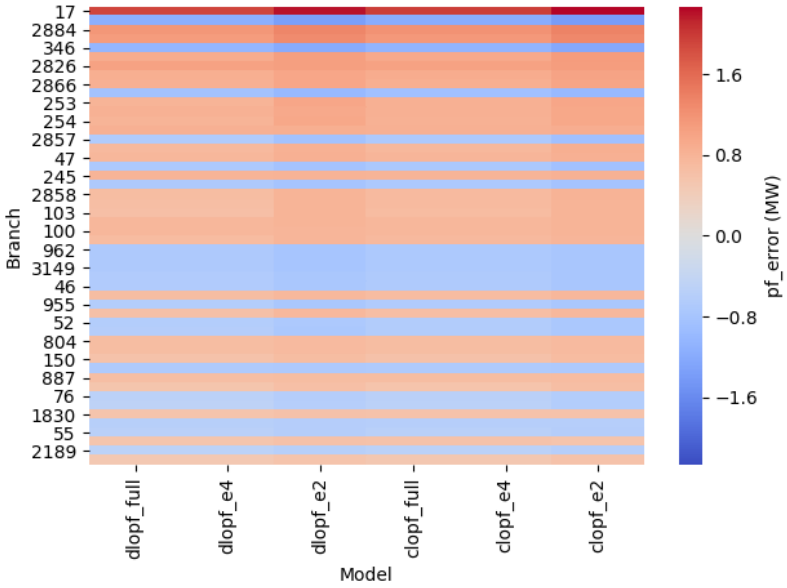

(b) case2737sop_k

Figure 10: Real power flow error in Polish test cases with factor truncation tolerances.

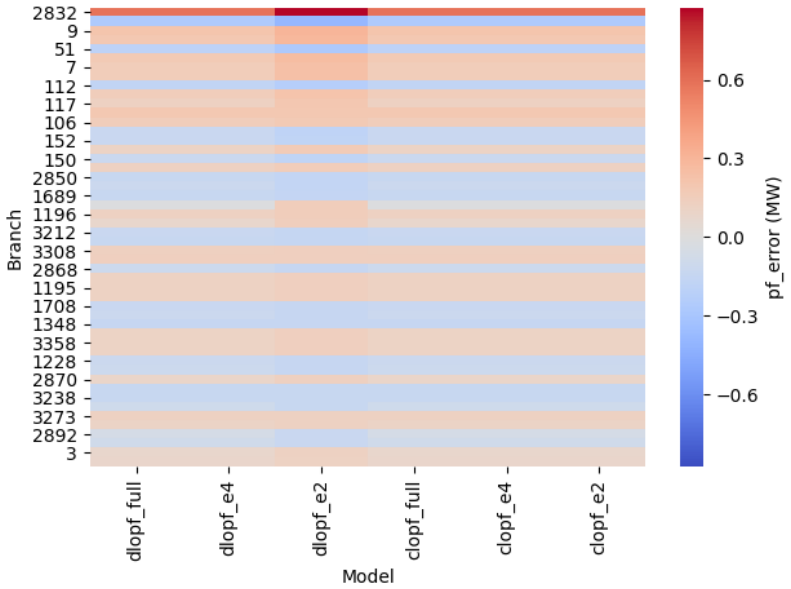

(c) case2746wop_k

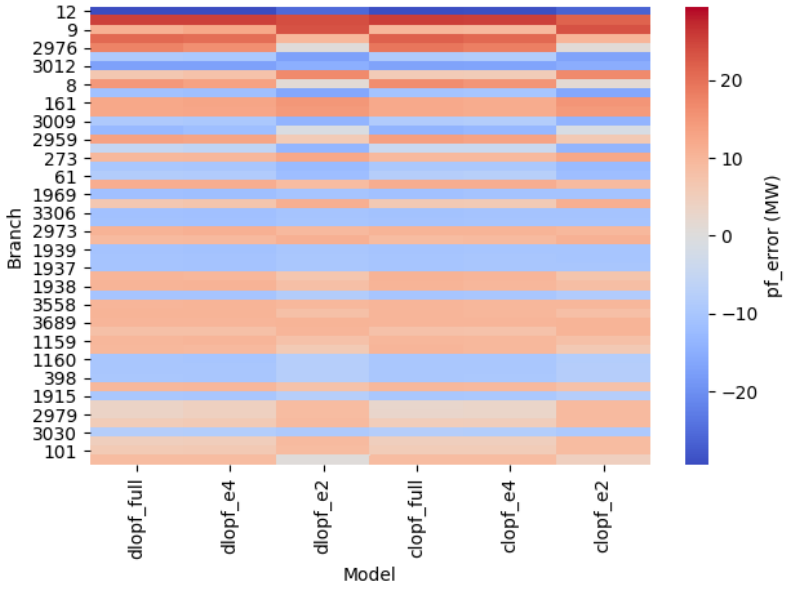

(d) case3120sp_k

Figure 10: Real power flow error in Polish test cases with factor truncation tolerances.

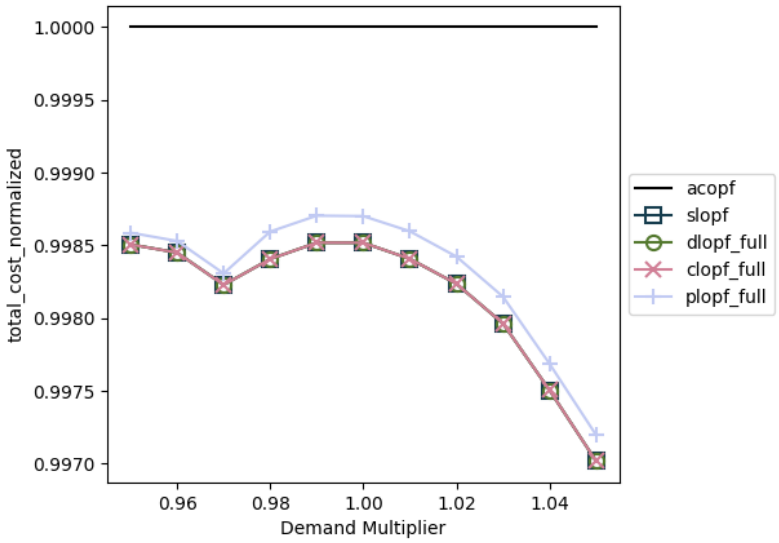

(a) Normalized total cost

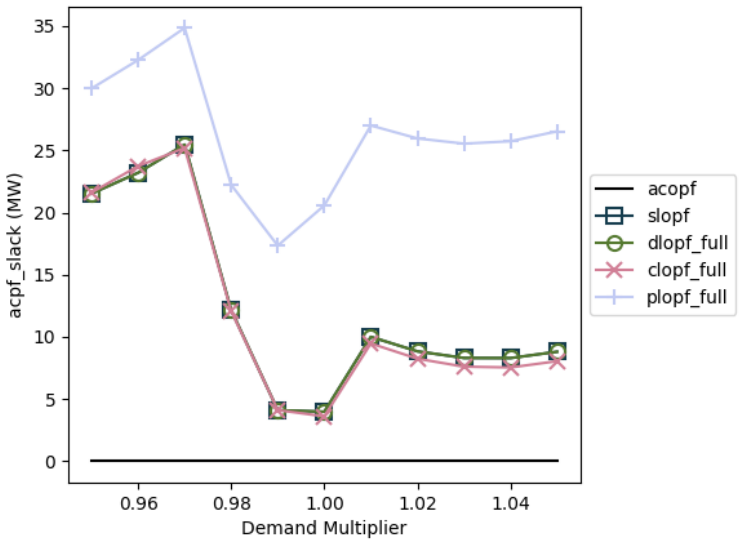

(b) Reference bus real power slack

Figure 11: Detailed error sensitivity analysis of the IEEE 118-bus test case.

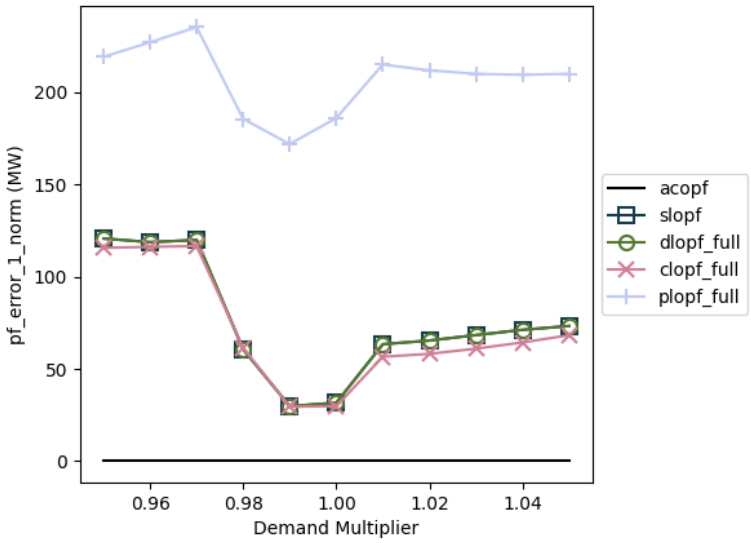

(c) Power flow error, 1-norm

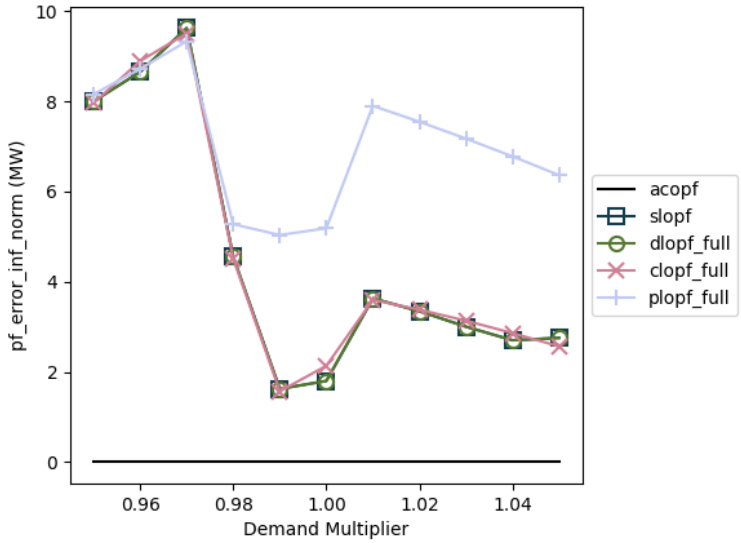

(d) Power flow error, ∞-norm

Figure 11: Detailed error sensitivity analysis of the IEEE 118-bus test case.

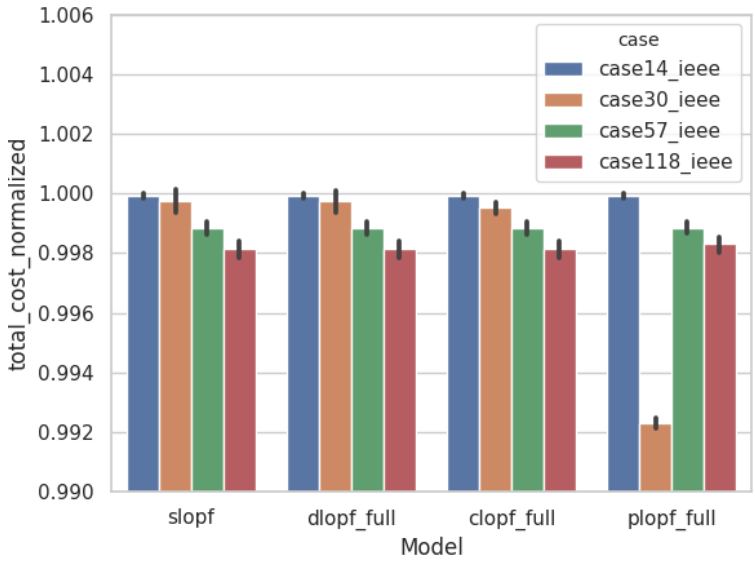

(a) Normalized total cost

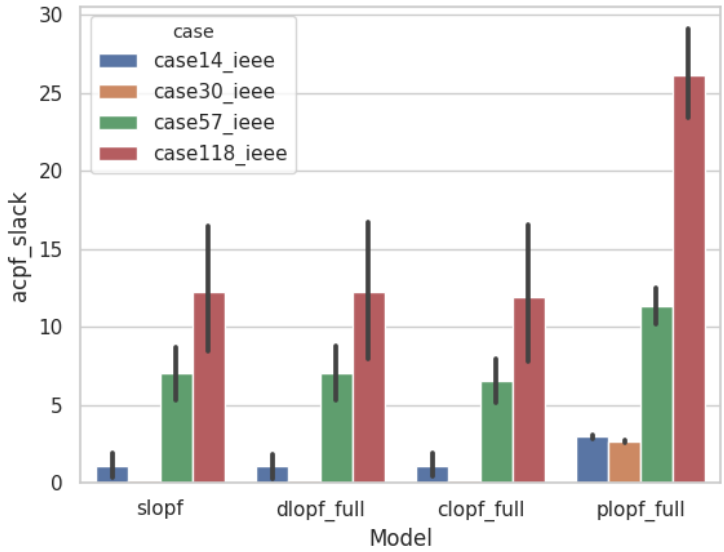

(b) Reference bus real power slack

Figure 12: Summary error sensitivity analysis of the IEEE test cases.

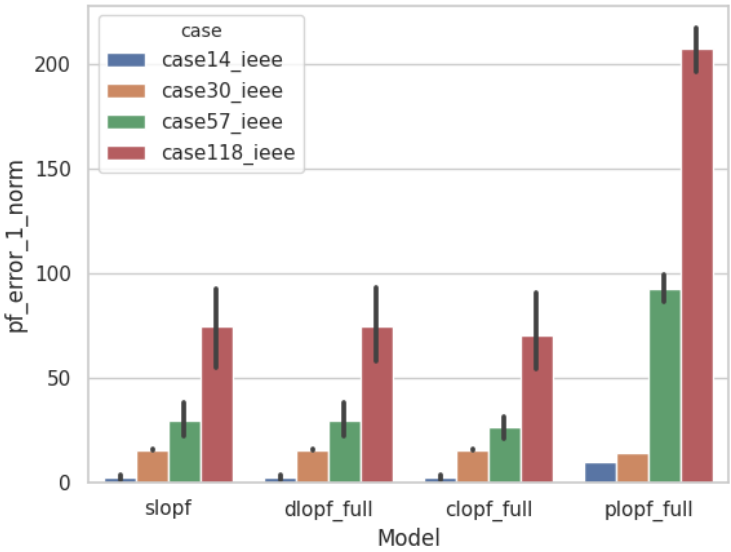

(c) Power flow error, 1-norm

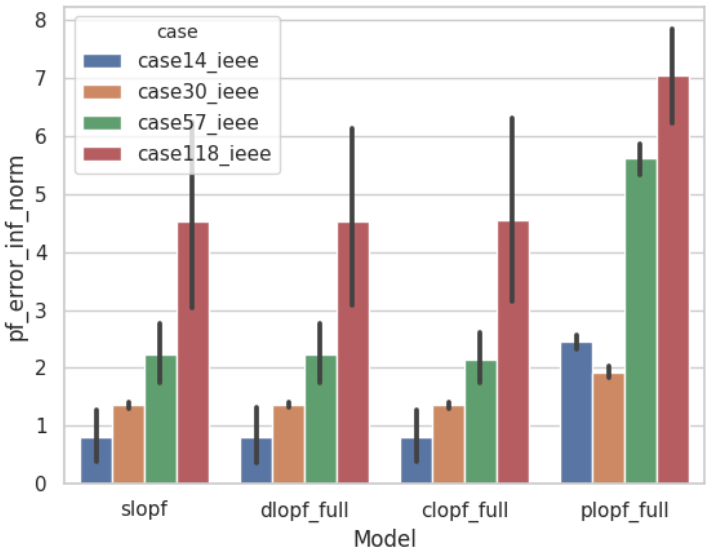

(d) Power flow error, ∞-norm

Figure 12: Summary error sensitivity analysis of the IEEE test cases.

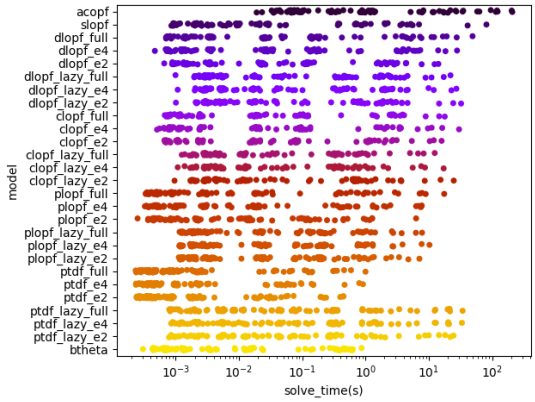

(a) All Cases

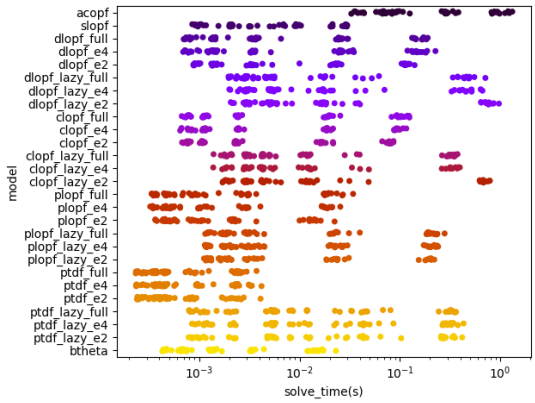

(b) IEEE Test Cases

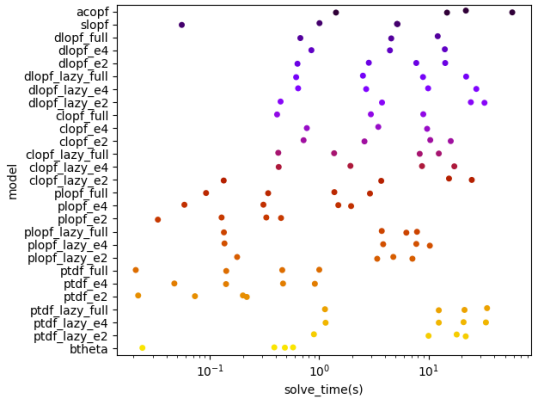

(c) SDET Test Cases

Figure 13: Solution times in all test cases and model implementations.

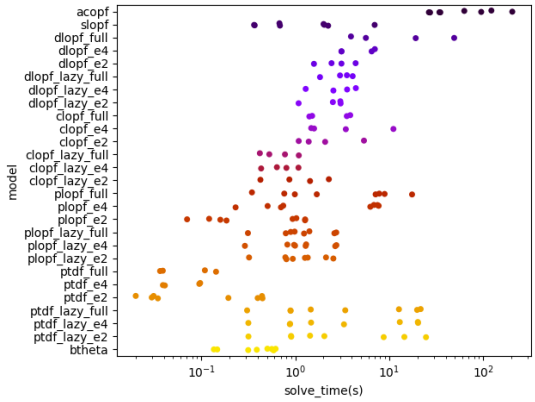

(d) RTE Test Cases

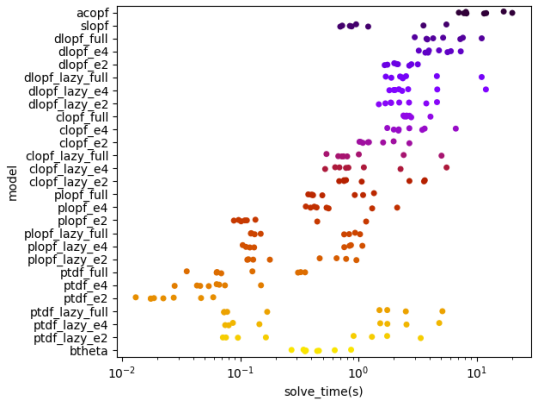

(e) Polish Test Cases

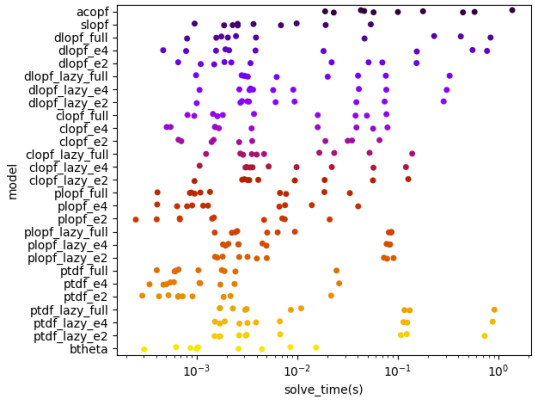

(f) MISC Test Cases

Figure 13: Solution times in all test cases and model implementations.

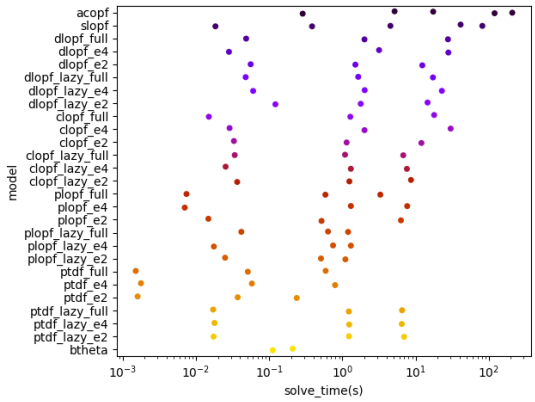

(g) PEGASE Test Cases

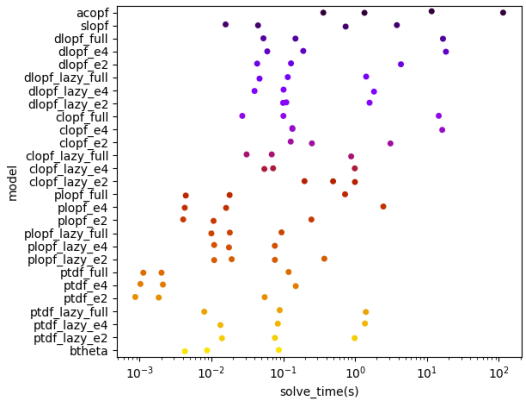

(h) TAMU Test Cases

Figure 13: Solution times in all test cases and model implementations.